

The power spectrum of galaxies from large to small scales: a line-intensity mapping perspective

Rui Lan Jun¹ , Tom Theuns² , Kana Moriwaki^{1,3} , Sownak Bose² 

¹ *Department of Physics, Graduate School of Science, The University of Tokyo, 7-3-1 Hongo, Bunkyo, Tokyo 113-0033, Japan*

² *Institute for Computational Cosmology, Durham University, South Road, Durham DH1 3LE, UK*

³ *Research Center for the Early Universe, Graduate School of Science, The University of Tokyo, 7-3-1 Hongo, Bunkyo, Tokyo 113-0033, Japan*

Accepted XXX. Received YYY; in original form ZZZ

ABSTRACT

We model the power spectrum of galaxies in the ILLUSTRISTNG simulation when they are weighted by their star formation rate. Such a weighting is relevant in the context of line-intensity mapping (LIM). On intermediate to large scales, the model accounts for non-linear bias of star-forming galaxies and halo exclusion (a 2-halo term). On small scales, it incorporates the weighted distribution of satellite galaxies within haloes (a 1-halo term). The random sampling of satellite galaxies adds a shot noise term to the power spectrum on small scales, and their confinement to haloes introduces a halo shot noise term on large scales. The full model reproduces the measured power spectrum to within a few per cent on all scales, and the fitting parameters have a clear physical meaning. Omitting satellite galaxies from the analysis leads to an underestimation of both the large-scale bias and the mean LIM intensity by ~ 30 per cent each at $z \sim 1.5$. Assigning the LIM intensity of satellites to the centre of their respective haloes affects the power spectrum on scales $k \gtrsim 0.3 \text{ h Mpc}^{-1}$. We discuss how the LIM power spectrum can be used to constrain cosmology on large scales, and galaxy formation on smaller scales, with our fitting function providing an accurate and well-motivated parametrisation.

Key words: methods: numerical – cosmology: large-scale structure of Universe – galaxies: star formation

1 INTRODUCTION

The distribution of galaxies in the Universe forms a web-like structure known as the cosmic web. This ‘large-scale’ structure resembles the patterns predicted by cosmological simulations of structure formation, under the assumption that galaxies inhabit dark matter haloes (e.g. Springel et al. 2005a). The presence of such dark matter haloes is consistent with measurements from gravitational lensing (Brainerd et al. 1996, see also Clampitt et al. 2017 and references therein). In the simulations, the pattern emerges through the gravitational amplification of initially small Gaussian perturbations imprinted in the initial conditions.

The perturbations themselves are thought to originate from quantum fluctuations in an inflaton field (Guth & Pi 1982) that were stretched to macroscopic scales during a brief epoch of cosmic inflation in the very early Universe (Guth 1981; Linde 1982; see, e.g., Liddle & Lyth 2000 for a more general review of inflation). This general framework for the origin of structure manages to describe both the cosmic microwave background (e.g. Planck Collaboration et al. 2020) and the observed large-scale structure, but direct evidence that inflation occurred is lacking. Deviations from the vanilla model of structure formation, such as non-Gaussian primordial fluctuations, and details of inflation may leave observational signatures that could be detected on scales that are sufficiently large that they are not affected by the nonlinearity associated

with gravitational growth (see, e.g., Cabass et al. 2023). The detection of such features may put the inflationary paradigm on firmer footing. Several large-scale surveys to collect the required data are underway (see, e.g., Ballardini et al. 2024 for the EUCLID survey). However, the detailed mapping of the Universe required on such large scales is a huge endeavour.

Line-intensity mapping (hereafter LIM) is an emerging observational technique which promises to map large volumes efficiently (for more details on LIM and reviews of surveys in preparation; see, e.g., Kovetz et al. 2017). The method takes advantage of the fact that many galaxies are bright in characteristic emission lines – for example the $n = 3 \rightarrow 2 \text{ H}\alpha$ line in H II. A LIM survey then consists of making a low-resolution spectrum of ‘voxels’ on the sky at sufficient depth to detect the emission line. Detecting the line not only reveals the presence of a galaxy, but the observed wavelength immediately yields its redshift as well.

Galaxies that are too faint to detect individually may nevertheless contribute to the line flux in a LIM voxel. A LIM survey may therefore be used to study the distribution of galaxies on very large scales, which is interesting from a cosmological perspective, but also on smaller, non-linear scales, which may be more relevant to the field of galaxy formation and evolution. In this sense, LIM provides a ‘full-shape’ measurement of the distribution of galaxies, from larger linear scales, to smaller non-linear scales.

Inferring cosmological parameters from a galaxy or LIM survey requires a model that relates dark matter haloes to the properties of the galaxies they host. This is far from trivial because the stellar mass or luminosity of a galaxy is not simply proportional to its halo mass.

The ‘Halo Occupation Distribution’ model (HOD, [Berlind & Weinberg 2002](#)) can be used to describe galaxy distributions in galaxy surveys (e.g. [Yuan et al. 2024](#), for DESI; [DESI Collaboration et al. 2016](#)). The HOD describes the galaxy-halo connection in terms of the conditional probability, $P(N|M_h)$, that a halo of mass M_h contains N galaxies. This statistical technique enables efficient creation of mock galaxy surveys based on the positions of haloes from dark matter-only simulations. Varying the HOD and the cosmological parameters of the simulation simultaneously yields constraints on the observed large-scale structure (e.g. [Yuan et al. 2024](#)).

HOD models have been applied to LIM in several studies ([Wyithe & Brown 2010](#); [Sun et al. 2019](#); [Wolz et al. 2019](#)). A LIM survey differs from a more traditional galaxy survey in that galaxies are *weighted* by the line’s luminosity. Most LIM line fluxes such as H α depend on the star formation rate (SFR) and hence galaxies with high SFR contribute more to the LIM signal than those with lower SFR. This weighting also means that the physics of galaxy formation – for example, the decrease in SFR when a central galaxy becomes a satellite after a halo merger, or the suppression of the SFR of a galaxy due to the activity of its central active galactic nucleus (AGN) – will also impact the LIM signal. It is unclear whether HOD modelling would be able to capture such details.

A more comprehensive approach towards modelling the galaxy formation process is offered by hydrodynamical simulations, a field in which there has been substantial progress in the last decade or so. There is now a range of models in the literature (e.g. [Vogelsberger et al. 2014](#); [Dubois et al. 2014](#); [Schaye et al. 2015](#); see [Vogelsberger et al. 2020](#) for a review) that approach the modelling of physical processes such as cooling, star formation, feedback from stars and black holes in various ways, demonstrating impressive consistency with the observed galaxy population for many observed properties. On the other hand, the use of hydrodynamical simulations in the context of cosmological analyses is somewhat hampered by their computational complexity and (comparatively) limited volume. While recent advances have been made to push hydrodynamical simulations into the regime relevant for large-scale galaxy surveys (see, e.g., [Pakmor et al. 2023](#); [Schaye et al. 2023](#)), the volumes achieved in these calculations are substantially smaller than those that will be probed by future LIM experiments. In this arena, ‘hybrid’ models – that blend the computational efficiency of dark matter-only simulations or semi-analytic methods with the predictions of hydrodynamical simulations – can be particularly informative.

It is common in LIM to connect galaxies to haloes by assuming a luminosity-halo mass relation. This relationship can be modelled directly based on the predictions of modern cosmological, hydrodynamical simulations. Often, no distinction is made between central and satellite galaxies (e.g. [Fonseca et al. 2016](#); [Gong et al. 2017](#); [Silva et al. 2017](#)), with the ‘Santa Cruz’ semi-analytical model suggesting that satellites contribute less than 10 per cent to the LIM signal ([Zhang et al. 2023](#)). If satellites are accounted for, then their spatial distribution in a halo is commonly modelled by assuming they follow a given density profile, for example that of Navarro,

Frenk & White (NFW, [Navarro et al. 1997a](#)); see, e.g., [Padmanabhan et al. 2017](#); [Wolz et al. 2019](#); [Schaan & White 2021](#).

While LIM surveys are not yet competitive with current large galaxy surveys in terms of cosmological constraints, near-future LIM surveys may be able to complement galaxy surveys on smaller scales by detecting previously missed galaxies. LIM surveys such as COPPS II ([Keating et al. 2016](#)) have already provided preliminary results on scales $k = 0.5\text{--}2$ h Mpc $^{-1}$ (where k is the comoving wavenumber), albeit with low signal-to-noise ratio. This scale corresponds to the non-linear regime which can be investigated using current hydrodynamical simulations (e.g. [Artale et al. 2017](#)). Current and upcoming LIM surveys (e.g. TIM ([Vieira et al. 2020](#)), SPHEREX ([Doré et al. 2018](#)), SPT-SLIM ([Karkare et al. 2022](#)), COMAP ([Karkare et al. 2022](#)), HETDEX ([Gebhardt et al. 2021](#)), MMIME ([Keating et al. 2020](#))) will further probe these non-linear scales.

Although taken into account in N -body simulations (e.g. [Springel et al. 2005b](#)), which solve equations of gravity numerically, semi-analytical models struggle to model the non-linear transition regime between the 2-halo and 1-halo terms. While the nonlinearity of galaxy clustering within haloes is captured in the 1-halo term, additional nonlinearities due to halo exclusion and non-linear halo clustering outside the scale of the size of haloes have also been found. Such effects need to be accurately modelled to understand the power spectrum in this intermediate regime, where linear theory does not apply. Deviations from the linear bias model (e.g. [Smith et al. 2007](#); [Hand et al. 2017](#); [Mead & Verde 2021](#)) and effects of halo exclusion (e.g. [Baldauf et al. 2013](#); [van den Bosch et al. 2013](#); [García & Rozo 2019](#)) have been actively studied in the context of galaxy surveys.

Effects of nonlinearity have also been studied in the context of LIM. [Pénin et al. \(2018\)](#) showed that, in 21-cm LIM, there is a coupling between small and large-scale modes, and the non-linear HI distribution contributes to the power spectrum on large scales. Because of this, the effective bias has a scale dependence even on large scales and could affect the constraints obtained from BAO signals and constraints on primordial non-Gaussianity ([Umeh et al. 2016](#); [Umeh 2017](#)). In [Villaescusa-Navarro et al. \(2018\)](#), the non-linearity of the 21-cm power spectra at $z < 5$ has been investigated using the ILLUSTRISTNG hydrodynamical simulation. [Moradinezhad Dizgah et al. \(2022\)](#) also discuss such effects in the context of CO and [CII] LIM using halo models.

The aim of this paper is to make some progress in understanding how the physics of galaxy formation might affect LIM on large scales, and what the small-scale LIM signal may tell us about the distribution of SFR within haloes. To this end, we study the power spectrum of galaxies weighted by their SFR extracted from the ILLUSTRISTNG simulations ([Nelson et al. 2017](#); [Springel et al. 2017](#); [Pillepich et al. 2018](#); [Marianacci et al. 2018](#); [Nelson et al. 2019](#)). We describe the measured power spectrum with a model that includes a bias of star-forming galaxies compared to a matter power spectrum on large scales (a 2-halo term), and a model for the distribution of satellite galaxies in haloes on smaller scales (a 1-halo term). The theoretical description is motivated by the halo model for the matter power spectrum ([Cooray & Sheth 2002](#)). Our model also accounts for scale-dependent shot noise, non-linear clustering and halo exclusion, motivated by [Baldauf](#)

et al. (2013). The paper is organised as follows: Section 2 presents the theory behind the model for the power spectrum; Section 3 briefly describes the ILLUSTRISTNG simulations, with Section 4 quantifying the impact of satellites on the power spectrum. We compare the model for the power spectrum to that obtained from the simulations, and provide fits for the 2-halo and 1-halo terms, in Section 5. We summarise our findings in Section 6.

Our investigation in this paper is not limited to a specific emission line but we pick $H\alpha$ at $z \sim 1$ as an example. Most of our results will also apply to other emission lines, provided the line luminosity is proportional to the galaxy’s SFR. For simplicity, we ignore contamination from continuum emission and from galaxies at other redshifts whose emission lines redshift to the same observed wavelength as the target line (line interlopers; see, e.g., Gong et al. 2020).

2 WEIGHTED POWER SPECTRUM: THEORY

The power spectrum provides a statistical description of the spatial distribution of a quantity, such as matter, galaxies, or the intensity of an emission line. In galaxy surveys, selected galaxies are typically weighted equally, but in LIM, galaxies contribute with a weight, W , that is proportional to the line flux. How does this weighting affect the power spectrum?

Galaxies are hosted by dark matter haloes, with more massive haloes containing a central galaxy and several satellite galaxies. We will show later (Section 3) that about 30 per cent of the cosmic star formation at redshift $z \sim 1$ occurs in satellites – and hence about 30 per cent of the total intensity detected in LIM is from satellites. How do satellites affect the LIM power spectrum?

In the following subsections, we present analytical calculations of the power spectrum to try to address these questions. The weight, W , remains general: it could be the galaxy’s SFR, the line flux, or some other quantity.

We expect that the power spectrum contains a term due to the clustering of the haloes and a term that describes the distribution of satellites in haloes. These two terms are reminiscent of the 2-halo and 1-halo terms of the *halo model*, a model that describes the power spectrum of the mass distribution measured in simulations (Cooray & Sheth 2002).

However, haloes are, at best, discrete tracers of the matter density field. Tracers that randomly (Poisson) sample a continuous distribution generate an extra ‘shot noise’ term in the measured power spectrum, a term named after Schottky, who studied this phenomenon in the context of electrical currents (Schottky 1918; see Schottky 2018 for a recent translation of the original paper). The expression for this shot noise contribution will need to account for the fact that not all haloes are weighted equally. Poisson sampling may be a good approximation on large scales, but not on scales comparable to or smaller than the radii of haloes, because haloes cannot overlap with each other – and hence are perfectly *anti-correlated* on those small scales. We will investigate how this ‘halo exclusion’ affects the power spectrum. (Stating that haloes cannot overlap is more than a theorist’s prejudice of how mass is distributed. For example, a galaxy’s SFR – and hence its weight – is strongly affected when it becomes a satellite.)

On scales smaller than the typical halo radius, we expect that the power spectrum depends on how satellites are dis-

tributed in haloes. For example, they might follow an NFW profile. Galaxies are discrete tracers of such a profile, resulting in a galaxy shot noise term.

In summary, we expect the galaxy power spectrum to be of the form

$$P_{\text{tot}}^{\text{gal}}(k) = \underbrace{P_{2h}(k, \hat{v}_h^{(s)}(\mathbf{k}))}_{\text{2-halo term}} + \underbrace{U(k)^2 (P_{\text{shot}}^{\text{halo}} - P_{\text{shot}}^{\text{gal}}) + P_{\text{shot}}^{\text{gal}}}_{\text{1-halo term}}, \quad (1)$$

and we will take a closer look at each term in the following subsections. Both $\hat{v}_h^{(s)}(\mathbf{k})$ and $U(k)$ depend on the distribution of weights within haloes. Figure 1 shows the power spectrum from the hydrodynamical simulation ILLUSTRISTNG, broken down into these terms (open circles). The model we propose in Section 5 is also plotted for comparison (solid lines). The first term, $P_{2h}(k, \hat{v}_h^{(s)}(\mathbf{k}))$, (orange) is the 2-halo term that results from the clustering of haloes, and our derivation will account for non-linear halo bias and halo exclusion, described in Section 2.3, as well as the contribution due to $\hat{v}_h^{(s)}(\mathbf{k})$, described in Section 2.4.1. The second and third terms make up the 1-halo term (red), which tends to the halo Poisson shot noise, $P_{\text{shot}}^{\text{halo}}$, (orange dash-dotted line) on large scales and the galaxy Poisson shot noise, $P_{\text{shot}}^{\text{gal}}$, (blue dash-dotted line) on small scales. The origin of this term is described in Section 2.4.2. The commonly used linear (dotted black) and non-linear (dashed black) power spectra are also shown in Fig. 1 for reference to illustrate that these models do not provide good approximations for the 2-halo term on smaller scales. On the other hand, the bottom panel of Fig. 1 shows that our proposed model agrees with the ILLUSTRISTNG power spectrum to within 15 per cent on all scales.

In this paper we use the Fourier convention of Peebles (1980): the Fourier transform pair f and \hat{f} are related by

$$\begin{aligned} \hat{f}(\mathbf{k}) &= \frac{1}{V} \int d\mathbf{r} \exp(-i\mathbf{k} \cdot \mathbf{r}) f(\mathbf{r}) \\ f(\mathbf{r}) &= \frac{V}{(2\pi)^3} \int d\mathbf{k} \exp(i\mathbf{k} \cdot \mathbf{r}) \hat{f}(\mathbf{k}). \end{aligned} \quad (2)$$

f and its Fourier transform \hat{f} have the same dimension. The power spectrum is $P(k) = V \langle |\hat{f}(k)|^2 \rangle$, where the angular brackets $\langle \cdot \rangle$ denote an ensemble average. In these expressions, $V = L^3$, where L is a comoving length on which f is periodic. In the case of simulations, L is the linear extent of the simulation volume. As pointed out by Kaiser & Peacock (1991), L does not appear in any comparison with data, and many papers set $L \rightarrow 1$, but we will not do so here.

In the following subsections, we will derive Eq. (1) following closely the derivation by Baldauf et al. (2013). Figure 2 illustrates schematically some of the steps involved. The left panel is the case of Eq. (1), in which a halo is resolved in terms of a central galaxy and its satellites, all with their own weight. The right panel is a simplification, where the weights of satellite and central galaxies are summed and placed at the position of the central galaxy (the ‘halo’ case). We refer to the power spectrum computed for the case of the left panel as the ‘galaxy power spectrum’, and that for the right panel as the ‘halo power spectrum’. The latter is where we start.

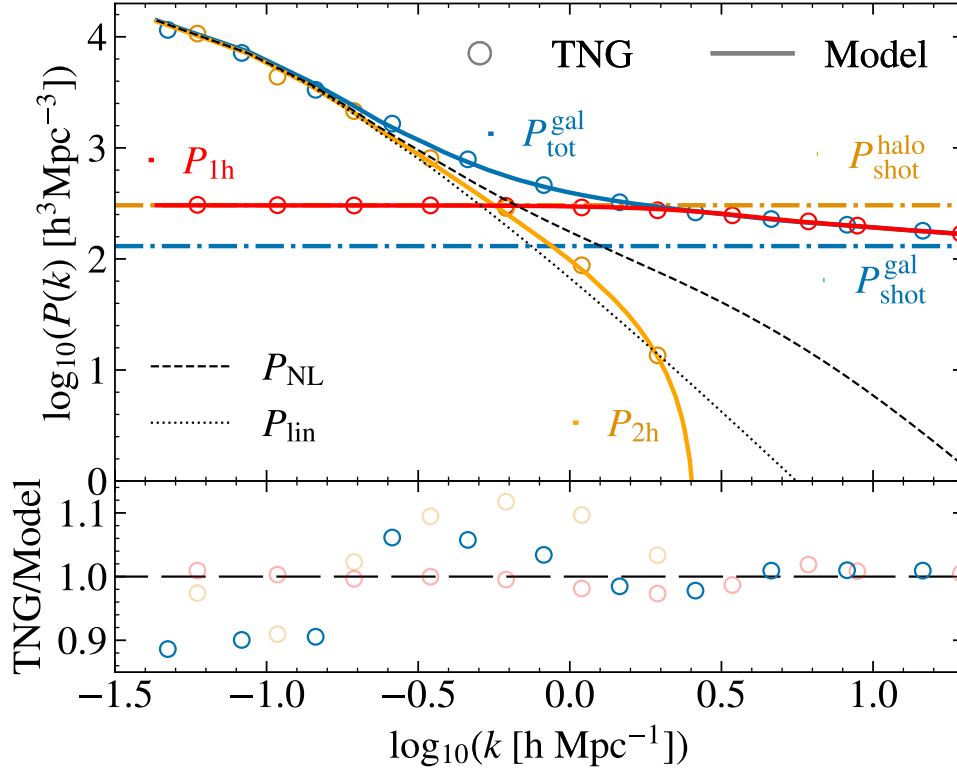


Figure 1. *Upper panel:* The components of the TNG galaxy power spectrum and the model proposed in this paper. *Open circles* correspond to TNG, and *solid lines* correspond to the model. *Blue* corresponds to the total power spectrum, while *orange* and *red* correspond to the 2-halo and 1-halo terms, respectively. The *orange* and *blue dash-dotted* lines show the Poisson shot noise computed using the luminosities of haloes and galaxies respectively. The *red line* tends to the halo shot noise on large scales and the galaxy shot noise on small scales. The non-linear (*dashed black*) and linear matter power spectra (*dotted black*) are plotted for reference. For $-0.5 \lesssim \log(k [\text{h Mpc}^{-1}]) \lesssim 0$, neither the 1-halo term nor the 2-halo term dominates. *Lower panel:* The ratio of the TNG power spectra to that of the model. The model proposed in this paper agrees with the TNG power spectrum to within 15 per cent on all scales. On the largest scales the TNG power spectrum is affected by sample variance, causing it to deviate from the fit. The fit is significantly better on scales $\log(k [\text{h Mpc}^{-1}]) \gtrsim -0.5$.

2.1 Power spectrum of a weighted distribution

The weight distribution of discrete, point-like objects can be written as

$$w(\mathbf{r}) = \sum_i W_i \delta^{(\text{D})}(\mathbf{r} - \mathbf{r}_i), \quad (3)$$

where W_i and \mathbf{r}_i are the weights and positions of each object, and $\delta^{(\text{D})}$ is the Dirac delta function. It is common to define the overdensity

$$\delta_w(\mathbf{r}) = \frac{w(\mathbf{r})}{\bar{w}} - 1, \quad (4)$$

where $\bar{w} = \sum_i W_i / V$.

The Fourier transform of Eq. (3) is

$$\begin{aligned} \hat{w}(\mathbf{k}) &= \frac{1}{V} \int d\mathbf{r} w(\mathbf{r}) \exp(-i\mathbf{k} \cdot \mathbf{r}) \\ &= \frac{1}{V} \sum_i W_i \exp(-i\mathbf{k} \cdot \mathbf{r}_i), \end{aligned} \quad (5)$$

giving the Fourier transform of $\delta_w(\mathbf{r})$ as

$$\hat{\delta}_w(\mathbf{k}) = \frac{\hat{w}(\mathbf{k})}{\bar{w}} - \hat{\delta}^{(\text{D})}(\mathbf{k}). \quad (6)$$

The delta function in Fourier space, $\hat{\delta}^{(\text{D})}(\mathbf{k})$, is only non-zero

for $k = 0$, where the power spectrum is 0. We will ignore this term in what follows.

The power spectrum of δ_w is

$$P_{\text{tot}}(k) = V \langle \hat{\delta}_w(\mathbf{k}) \hat{\delta}_w(-\mathbf{k}) \rangle. \quad (7)$$

Although $\langle \cdot \rangle$ is meant to be the average over all possible outcomes of a stochastic process, we can only average over what we can measure. When applied to simulations in the next section, we average over all the \mathbf{k} 's in a bin of wavenumber. The larger the number of \mathbf{k} 's in each bin, the closer we expect to be to the ensemble average. For small $|\mathbf{k}|$, the simulation volume samples few independent \mathbf{k} 's, and our measurement is affected by sample variance.

For LIM, W_i would be the flux F_i of an object at position \mathbf{r}_i . If all the objects are at the same redshift, then flux weighting is equivalent to luminosity weighting, except for the differences in the overall scaling factor. As we only consider one redshift at a time, we will consider luminosity in the rest of this paper. In LIM, \bar{w} is given by the *specific* mean intensity,

$$\bar{I} = \frac{\sum_i F_i}{d\Omega d\nu_{\text{obs}}} = \frac{\sum_i \frac{L_i}{4\pi D_L^2}}{d\Omega d\nu_{\text{obs}}}, \quad (8)$$

where F_i is the flux of each object, $d\Omega$ is the solid angle of the survey, and $d\nu_{\text{obs}}$ is the frequency corresponding to the

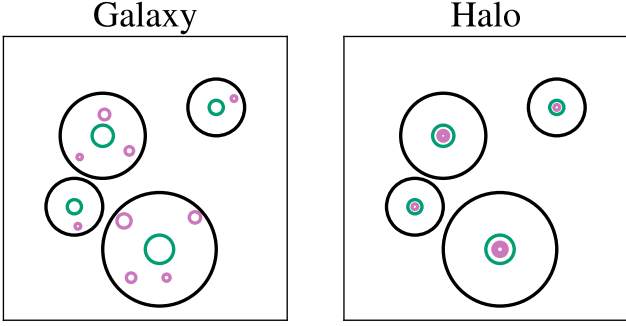


Figure 2. Schematic comparing two different ways to assign weights to galaxies in a dark matter halo. The *green circles* are each halo’s central galaxy and the *pink circles* denote satellites, with the radii of the circles being a measure of the weight assigned to the galaxy; the *black circles* show the virial radii of the haloes. **Left panel:** The resolved ‘galaxy’ case, in which central and satellites are at different locations. **Right panel:** The ‘halo’ case: the weights of central and satellites are added to the position of the central galaxy. In LIM, the individual weights are the line fluxes.

depth considered. L_i is the luminosity of each object and D_L is the comoving luminosity distance.

It is common in LIM to not divide by the mean intensity when computing the power spectrum, since the mean intensity may be difficult to measure. In this case, the power spectrum can be written as $P_{\text{tot},w}(k) = V \langle \hat{w}(\mathbf{k}) \hat{w}(-\mathbf{k}) \rangle$. In this paper, we use the subscript w (or I for intensity) to indicate the case of a field that is *not* normalised by its mean. Using Eq. (3), this power spectrum can be written as the sum of all the contributions:

$$P_{\text{tot},w}(k) = \frac{1}{V} \left\langle \sum_{i,j} W_i W_j \exp[-i\mathbf{k} \cdot (\mathbf{r}_i - \mathbf{r}_j)] \right\rangle, \quad (9)$$

where i and j run over all objects.

The total power spectrum can be separated into contributions from pairs between distinct objects and self-pairs:

$$P_{\text{tot},w}(k) = \frac{1}{V} \left\langle \sum_{i \neq j} W_i W_j \exp[-i\mathbf{k} \cdot (\mathbf{r}_i - \mathbf{r}_j)] \right\rangle + \frac{1}{V} \left\langle \sum_{i=j} W_i W_j \exp[-i\mathbf{k} \cdot (\mathbf{r}_i - \mathbf{r}_j)] \right\rangle. \quad (10)$$

In the simplest case, the first term describes clustering and the second term the shot noise. We describe these in more detail in the following subsection.

2.2 Clustering vs Shot noise

The power spectrum in Eq. (10) contains a clustering term and a shot noise term. The clustering term describes how objects are distributed relative to each other beyond what would be expected if they were randomly (Poisson) distributed. The shot noise contribution exists even if objects are randomly distributed.

Shot noise is statistical noise that arises due to the inherent randomness in the sampling of discrete objects from a probability distribution. If objects are sampled independently from a probability distribution, then the local number density of objects at each point can be considered to follow a Poisson distribution with mean proportional to the expected

number density at that point. Random sampling causes additional fluctuations in the density field, which manifests as the shot noise contribution to the power spectrum.¹ In this case, the resulting Poisson shot noise is given by the contribution from self-pairs in the power spectrum (the second term in Eq. (10)), while the clustering term is given by the contribution from distinct pairs (the first term in Eq. (10)).

Poisson sampling may not be a good approximation when objects are not sampled independently or there are additional constraints, such as halo exclusion (Section 2.3.2) or galaxies restricted to being within haloes (Section 2.4). In this case, the self-pair contribution may not fully describe the stochasticity. Nevertheless, the self-pair term still describes the power expected in the case of random distribution, and the distinct pair term still describes the additional fluctuation in the density field relative to that expected for a random distribution.

The second term in Eq. (10) can be simplified to

$$P_{\text{shot},w}(k) = \frac{1}{V} \sum_i W_i^2 = V \bar{w}^2 \frac{\sum_i W_i^2}{(\sum_i W_i)^2}. \quad (11)$$

For a standard galaxy survey, all selected galaxies are weighted equally, such that $W_i = 1$ for all objects and the shot noise tends to the inverse number density of galaxies, $1/\bar{n}$. The shot noise in the weighted case can be rewritten using the number density, \bar{n} , as follows:

$$\begin{aligned} P_{\text{shot},w} &= \bar{w}^2 V \frac{(\sum_i W_i^2)/N}{(\sum_i W_i)^2/N} \\ &= \bar{w}^2 V \frac{\langle W^2 \rangle}{N \langle W \rangle^2} \\ &= \frac{\bar{w}^2}{\bar{n}} \left(\frac{\text{Var}(W)}{\langle W \rangle^2} + 1 \right). \end{aligned} \quad (12)$$

We see that shot noise depends on the variance of the weights (i.e. luminosities in LIM). In standard galaxy surveys, the shot noise decreases when the number density of galaxies measured increases. In LIM, the shot noise additionally depends on the variance of the luminosities. When the power spectrum is not multiplied by the mean weight, the shot noise depends on the ratio of the variance of the weights over the square of their mean.

2.3 Halo Power Spectrum

In this subsection, we consider the power spectrum when using haloes as tracers of the matter distribution. In this paper, we take the halo power spectrum to be the case where the signal, i.e. the weight, is solely at halo centres (right panel of Fig. 2). This allows us to discuss the effects of non-linear bias and halo exclusion separately from the effects of galaxy

¹ Shot noise is sometimes confused with the noise introduced by a discrete representation of a continuous distribution. If discrete particles are placed deterministically to represent a continuous distribution with no sampling, then on large enough scales the power spectrum of the discrete particles will match that of the continuous distribution. However, the finite number of particles introduces noise on small scales, where the discrepancy between the discrete and continuous representations becomes noticeable. This differs from shot noise, which introduces noise on all scales due to random sampling.

distribution within each halo. This power spectrum is often computed for simplicity, to avoid having to model the 1-halo term, therefore it is important to understand the differences between the halo and galaxy power spectra.

The halo power spectrum is the sum of a term due to the clustering of pairs of haloes (the 2-halo term, P_{2h}^{halo}), and a shot noise term ($P_{\text{shot}}^{\text{halo}}$),

$$P_{\text{tot}}^{\text{halo}} = P_{2h}^{\text{halo}} + P_{\text{shot}}^{\text{halo}}. \quad (13)$$

This corresponds to the two terms in Eq. (10).

2.3.1 Non-linear halo bias

Haloes are biased tracers of the matter density, hence the power spectrum can be written as,

$$P_{\text{tot}}^{\text{halo}} = b_1^2 P_m + P_{\text{shot}}^{\text{halo}}, \quad (14)$$

where b_1 is the bias factor. The matter power spectrum, P_m , can be measured from N -body simulations that evolve an initially linear density field into the non-linear regime. Several fitting functions for P_m exist (e.g. HALOFIT; Takahashi et al. 2012), but there is no analytical form that works on all scales.

The matter power spectrum deviates from linear theory on small scales and at low redshifts, but the linear power spectrum is nevertheless useful since it can be described analytically. Therefore it is common to define halo bias with respect to the linear power spectrum P_{lin} :

$$P_{\text{tot}}^{\text{halo}} = b_2^2 P_{\text{lin}} + P_{\text{shot}}^{\text{halo}}. \quad (15)$$

In this case, the nonlinearities in the halo bias and in the matter power spectrum are both included in b_2 . Mo & White (1996) showed that the halo bias is scale-independent on sufficiently large scales. However, on scales comparable to the radii of haloes, b_2 becomes scale-dependent (Sheth & Tormen 1999; Jose et al. 2016). One reason is that the matter density field itself becomes non-linear. Such scale-dependence of the bias b_2 has been found to be more significant at higher redshifts, and weakens at lower redshifts (Sheth & Tormen 1999).

2.3.2 Halo exclusion

In addition to the nonlinearity, the standard halo model also fails to take into account the fact that haloes cannot be within a certain distance of each other. When there is a minimum distance between the luminosity signals due to the size of haloes, the so-called halo exclusion effect appears in the observed power spectrum. In the context of galaxy surveys, corrections to the power spectrum due to halo exclusion have been discussed by, e.g., Casas-Miranda et al. (2002); Smith et al. (2007); Baldauf et al. (2013).

The effect of halo exclusion can be understood more intuitively by looking at the correlation function, the Fourier transform of the power spectrum. For the weight distribution, the correlation function is defined as

$$\xi(r) = \langle \delta_w(\mathbf{r}_1) \delta_w(\mathbf{r}_2) \rangle, \quad (16)$$

where $r = |\mathbf{r}_1 - \mathbf{r}_2|$. We do not consider self-pairs in the correlation function, following the common practice in galaxy

survey analyses. Assuming that the minimum distance between all haloes is D , the correlation function is given by

$$\xi(r) = \begin{cases} -1 & \text{when } r < D \\ \xi'(r) & \text{when } r \gtrsim D, \end{cases} \quad (17)$$

where $\xi'(r)$ describes the clustering of haloes for scales larger than the exclusion distance, D . The correlation function given by Eq. (17) corresponds to the definition provided in Eq. (16), with self-pairs excluded.

If $\xi'(r)$ is defined for $r < D$, then it could be thought of as the *hypothetical* correlation function in the absence of halo exclusion. From the observed correlation function $\xi(r)$, as given by Eq. (17), it is not possible to infer what the correlation function would have looked like below the distance D in the absence of halo exclusion.

Fourier transforming Eq. (17) gives the power spectrum which takes into account halo exclusion for the case of a single exclusion distance D :

$$\begin{aligned} P_{2h}(k) &= \int_0^\infty \xi(r) \exp(-i\mathbf{k} \cdot \mathbf{r}) d^3r \\ &= 4\pi \int_0^\infty \xi(r) \frac{\sin(kr)}{kr} r^2 dr \\ &= -4\pi \int_0^D \frac{\sin(kr)}{kr} r^2 dr + 4\pi \int_D^\infty \xi'(r) \frac{\sin(kr)}{kr} r^2 dr, \end{aligned} \quad (18)$$

where the simplification to the second line assumes spherical symmetry.

In the more realistic case where there is a distribution of exclusion distances and the probability of finding a pair of haloes whose separation is larger than r is given by $f(r)$, the resulting correlation function is given by

$$\xi(r) = f(r) \xi'(r). \quad (19)$$

While in Eq. (17), the function $\xi'(r)$ needs only be defined above the exclusion distance D , in the case where there is more than a single exclusion distance, $\xi'(r)$ needs to be defined down to at least the smallest exclusion distance. Note that although this means that $\xi'(r)$ is defined below the scale of the size of larger haloes, this does not mean the halo profile is being probed. The small-scale contribution is due to smaller haloes being able to reside closer to other haloes.

The power spectrum for the more realistic case where there is a range of exclusion distances is given by

$$P_{2h}(k) = 4\pi \int_0^\infty f(r) \xi'(r) \frac{\sin(kr)}{kr} r^2 dr, \quad (20)$$

where $f(r)$ describes the probability distribution of finding a pair of haloes whose separation is larger than r in the absence of clustering.

As an example, consider the linear halo model to be the base model, with the power spectrum given by

$$b_2^2 P_{\text{lin}}(k) = 4\pi b_2^2 \int_0^\infty \xi_{\text{lin}}(r) \frac{\sin(kr)}{kr} r^2 dr. \quad (21)$$

In this case, the effect of exclusion can be included as follows:

$$P_{2h}(k) = 4\pi b_2^2 \int_0^\infty f(r) \xi_{\text{lin}}(r) \frac{\sin(kr)}{kr} r^2 dr. \quad (22)$$

Figure 3 shows the power spectrum for the case where halo exclusion is applied to the linear correlation function, assuming haloes have the same radii. The correlation function being

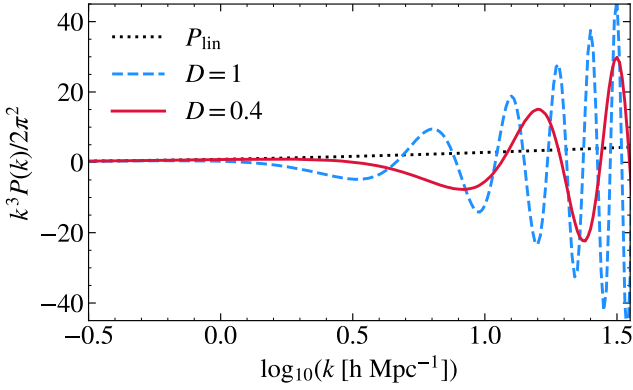


Figure 3. Halo exclusion applied to the linear correlation function, ξ_{lin} . The linear power spectrum is shown in *dotted black*. Equation (17) is shown for two exclusion distances, $D = 0.4 \text{ cMpc h}^{-1}$ (*solid red*) and $D = 1 \text{ cMpc h}^{-1}$ (*dashed blue*), with $\xi'(r)$ given by ξ_{lin} . The dimensionless power spectrum $k^3 P(k)/2\pi^2$ has been used to reduce the y-axis range.

Fourier transformed is given by Eq. (17) for two exclusion distances, $D = 0.4 \text{ cMpc h}^{-1}$ (solid red) and $D = 1 \text{ cMpc h}^{-1}$ (dashed blue), with ξ' given by the linear correlation function. The linear power spectrum with $b_2 = 1$ is shown in dotted black for reference. The halo exclusion creates wiggles in the power spectrum on small scales. The decrease in the power spectrum starts at lower k when the exclusion distance is larger.

The general form for the total power spectrum accounting for halo exclusion is

$$P_{\text{tot}}^{\text{halo}} = 4\pi \int_0^\infty f(r)\xi'(r) \frac{\sin(kr)}{kr} r^2 dr + P_{\text{shot}}^{\text{halo}}. \quad (23)$$

The non-linear bias discussed in Section 2.3.1 should be included in the $\xi'(r)$ function, while the distribution of exclusion distances is described by $f(r)$.

Baldauf et al. (2013) attempt to take into account the non-linear enhancement of clustering outside the exclusion radius by adding a non-linear contribution (a quadratic bias), but the resulting fit underestimates the power spectrum measured in their simulation (see their fig. 5). Mead & Verde (2021) provide a correction to the halo model which includes non-linear halo bias and halo exclusion in a single non-linear term calibrated using simulations. However, in this case the effects due to non-linear halo bias and halo exclusion are not distinguished. In Section 5.1, we show that the physically motivated formalism for halo exclusion presented in this subsection can be included in a fit to reproduce the 2-halo term measured in simulations.

In Section 2.2, we introduced shot noise as the contribution to the power spectrum arising from statistical fluctuations due to sampling from a probability distribution. As in Baldauf et al. (2013), we use the term stochasticity to refer more generally to statistical fluctuations due to random processes, contributing to the non-deterministic relation between the distribution of the tracers and the underlying probability distribution. Due to halo exclusion, haloes are not independently sampled from the probability distribution, as they must satisfy the additional condition of avoiding each other. Therefore, halo exclusion introduces an additional contribution to the stochasticity, in addition to the Poisson shot noise.

2.4 Galaxy power spectrum

Our formulation in the previous subsection has only considered haloes, but haloes are not observable. Often, tracers such as galaxies, which are hosted by haloes, are used.

Equation (9) can be decomposed into the contributions from pairs of galaxies in different haloes and pairs in the same halo as follows:

$$\begin{aligned} P_{\text{tot},w}^{\text{gal}}(k) &= P_{2h,w}^{\text{gal}}(k) + P_{1h,w}^{\text{gal}}(k) \\ &= \frac{1}{V} \left\langle \sum_{\substack{h,h' \\ h \neq h'}} \sum_{g \in h} \sum_{g' \in h'} W_g W_{g'} \exp[-i\mathbf{k} \cdot (\mathbf{r}_g - \mathbf{r}_{g'})] \right\rangle \\ &\quad + \frac{1}{V} \left\langle \sum_h \sum_{g \in h} \sum_{g' \in h} W_g W_{g'} \exp[-i\mathbf{k} \cdot (\mathbf{r}_g - \mathbf{r}_{g'})] \right\rangle, \end{aligned} \quad (24)$$

where h and h' are indices running over all the haloes, while g and g' run over all the galaxies in haloes. This decomposition is different from Eq. (10), where we decomposed the total power spectrum into contributions from pairs between distinct objects and self-pairs. In this paper, we take the first term of Eq. (24) to be the 2-halo term and the second term to be the 1-halo term. This means the 1-halo term here includes the galaxy shot noise (self-pairs of galaxies). Note that in terms of the correlation function, the 1-halo term often does not include the galaxy shot noise, since the correlation function used usually ignores self-pairs. It is also common in the literature to not include self-pairs in the 1-halo term in the power spectrum, and consider this as a separate shot noise term. We refrain from this practice in this paper, as this shot noise does not describe the shot noise on large scales, as we explain in Section 2.4.2.

To relate the Fourier transform of a density distribution, given by Eq. (5), to the distribution of galaxies within a halo, we write the transform as

$$\begin{aligned} \hat{w}(\mathbf{k}) &= \frac{1}{V} \exp(-i\mathbf{k} \cdot \mathbf{r}_h) \sum_i W_i \exp[-i\mathbf{k} \cdot (\mathbf{r}_i - \mathbf{r}_h)] \\ &\equiv \exp(-i\mathbf{k} \cdot \mathbf{r}_h) \hat{w}_h(\mathbf{k}), \end{aligned} \quad (25)$$

where \mathbf{r}_h denotes the halo centre, and we define $\hat{w}_h(\mathbf{k})$ as the Fourier transform of the distribution of galaxies within halo h :

$$\hat{w}_h(\mathbf{k}) = \frac{1}{V} \sum_i W_i \exp[-i\mathbf{k} \cdot (\mathbf{r}_i - \mathbf{r}_h)]. \quad (26)$$

We additionally define

$$\hat{v}_h^{(s)}(\mathbf{k}) = \frac{\sum_{g \in h} W_g \exp[-i\mathbf{k} \cdot (\mathbf{r}_g - \mathbf{r}_h)]}{\sum_{g \in h} W_g}, \quad (27)$$

which is the normalised Fourier transform of the weighted distribution of sampled galaxies. We use the superscript '(s)' (for 'sampled') to distinguish between the Fourier transform of a discrete, sampled distribution of galaxies, and the Fourier transform $\hat{u}(k)$ of the underlying function from which the galaxies are sampled. Their power spectra differ by a shot noise term.

2.4.1 2-halo term

The 2-halo, $P_{2h}(k)$, term in the galaxy power spectrum is largely the same as in the halo power spectrum, except that

it is influenced by $\hat{v}_h^{(s)}(\mathbf{k})$ on scales close to the size of haloes, where the variations in the distances between galaxies in a pair of haloes become noticeable.

The $\hat{v}_h^{(s)}(\mathbf{k})$ given by Eq. (27) can be substituted into the first term in Eq. (24) to give

$$\begin{aligned}
P_{2h,w}^{\text{gal}}(k) &= \frac{1}{V} \left\langle \sum_{\substack{h,h' \\ h \neq h'}} \sum_{g \in h} \sum_{g' \in h'} W_g W_{g'} \exp[-i\mathbf{k} \cdot (\mathbf{r}_g - \mathbf{r}_{g'})] \right\rangle \\
&= \frac{1}{V} \left\langle \sum_{\substack{h,h' \\ h \neq h'}} \sum_{g \in h} \sum_{g' \in h'} W_g W_{g'} \hat{v}_h^{(s)}(\mathbf{k}) \hat{v}_{h'}^{(s)}(\mathbf{k}) \exp[-i\mathbf{k} \cdot (\mathbf{r}_h - \mathbf{r}_{h'})] \right\rangle \\
&= \frac{1}{V} \left\langle \sum_{\substack{h,h' \\ h \neq h'}} W_h W_{h'} \hat{v}_h^{(s)}(\mathbf{k}) \hat{v}_{h'}^{(s)}(\mathbf{k}) \exp[-i\mathbf{k} \cdot (\mathbf{r}_h - \mathbf{r}_{h'})] \right\rangle,
\end{aligned} \tag{28}$$

where $W_h = \sum_{g \in h} W_g$ is the combined weight of all galaxies g in halo h . On large scales, $\hat{v}_h^{(s)}(\mathbf{k}) \rightarrow 1$, and the 2-halo term tends to the halo power spectrum, $P_{2h,w}^{\text{gal}}(k) \rightarrow P_{\text{tot},w}^{\text{halo}}(k)$.

The positions of the weights W will be affected by halo exclusion and non-linear bias as discussed in Section 2.3.1 and Section 2.3.2. It is also affected by how satellites are distributed inside their host haloes. We turn to this 1-halo term next.

2.4.2 1-halo term, including scale-dependent shot noise

The power spectrum of galaxies within the same halo (1-halo term, $P_{1h}(k)$) can be written in terms of the observed weight distribution of halos, $\hat{v}_h^{(s)}(\mathbf{k})$ (Eq. 27), as

$$\begin{aligned}
P_{1h,w}(k) &= \frac{1}{V} \left\langle \sum_h \sum_{g \in h} \sum_{g' \in h} W_g W_{g'} \exp[-i\mathbf{k} \cdot (\mathbf{r}_g - \mathbf{r}_{g'})] \right\rangle \\
&= \frac{1}{V} \left\langle \sum_h \sum_{g \in h} \sum_{g' \in h} W_g W_{g'} \hat{v}_h^{(s)}(\mathbf{k}) \hat{v}_h^{(s)}(-\mathbf{k}) \right\rangle \\
&= \frac{1}{V} \left\langle \sum_h \left(\sum_{g \in h} W_g \right) \left(\sum_{g' \in h} W_{g'} \right) |\hat{v}_h^{(s)}(\mathbf{k})|^2 \right\rangle \\
&= \frac{1}{V} \left\langle \sum_h W_h^2 |\hat{v}_h^{(s)}(\mathbf{k})|^2 \right\rangle.
\end{aligned} \tag{29}$$

$P_{1h,w}(k)$ tends to the halo shot noise, Eq. (11), when $k \gg 1/R$, with R the virial radius of the largest halo, since $\hat{v}_h^{(s)}(\mathbf{k}) \rightarrow 1$.

Galaxies sample the halo profile discretely, generating a shot noise term in $|\hat{v}_h^{(s)}(\mathbf{k})|^2$. This shot noise term corresponds to the part of the double sum with $g = g'$ in the above expression, with the $g \neq g'$ term describing the underlying halo profile. We describe the latter by defining

$$|\hat{u}_h(k)|^2 = \frac{\left\langle \sum_{g \in h} \sum_{g' \neq g \in h} W_g W_{g'} \exp[-i\mathbf{k} \cdot (\mathbf{r}_g - \mathbf{r}_{g'})] \right\rangle}{\sum_{g \in h} \sum_{g' \neq g \in h} W_g W_{g'}}. \tag{30}$$

The 1-halo term can also be separated into self-pairs and distinct pairs, yielding (see Appendix A1 for details)

$$\begin{aligned}
P_{1h}^{\text{gal}}(k) &= U(k)^2 (P_{\text{shot}}^{\text{halo}} - P_{\text{shot}}^{\text{gal}}) \\
&\quad + P_{\text{shot}}^{\text{gal}},
\end{aligned} \tag{31}$$

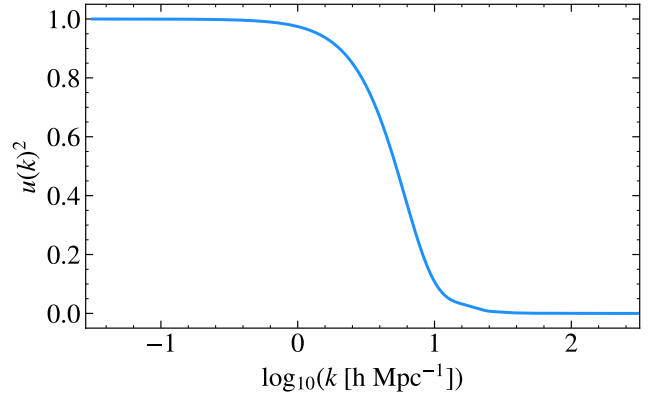


Figure 4. Power spectrum of the halo profile, $\hat{u}(k)^2$, assuming galaxies follow an NFW profile with scale radius $r_s = 0.125$ cMpc h^{-1} and virial radius $r_{\text{vir}} = 0.5$ cMpc h^{-1} . $\hat{u}(k)$ tends to 1 on scales $\gg 1/r_{\text{vir}}$ and to 0 on scales $\ll 1/r_s$.

where $U(k)^2$ is defined as

$$U(k)^2 = \frac{\sum_h (W_h^2 - \sum_{g \in h} W_g^2) |\hat{u}_h(k)|^2}{\sum_h (W_h^2 - \sum_{g \in h} W_g^2)}. \tag{32}$$

This gives us the second term of Eq. (1). Since each $|\hat{u}_h(k)|^2 \rightarrow 1$ as $k \rightarrow 0$, and $|\hat{u}_h(k)|^2 \rightarrow 0$ as $k \rightarrow \infty$ (given that $u_h(r)$ are integrable functions), $U(k)$ follows the same trends. This means that the 1-halo term, $P_{1h}^{\text{gal}}(k)$, tends to the halo shot noise on large scales and the galaxy shot noise on small scales.

The $\hat{u}_h(k)$ in Eq. (30) corresponds to the Fourier transform of the density profile of the halo if all galaxies have the same weight. In Appendix A2, we discuss the physical interpretation of $\hat{u}_h(k)$ when the weights are not the same.

Figure 4 shows $\hat{u}_h(k)^2$, where $\hat{u}_h(k)$ is the Fourier transform of an NFW profile (with $r_s = 0.125$ cMpc h^{-1} and $r_{\text{vir}} = 0.5$ cMpc h^{-1}). For a realistic sample of haloes, the haloes will not all have the same halo profile, therefore $U(k)^2$ will be a weighted average of (the Fourier transforms of) the (weighted) halo profiles of each halo, given by Eq. (32).

The location of the central galaxy is not sampled from a density distribution – it is fixed at the ‘centre’ – hence central and satellites should be treated differently. We show the formalism for the case where $\hat{u}_{\text{sat}}(k)$ describes the distribution of satellite galaxies only, in Appendix B.

In galaxy surveys, observing more galaxies is expected to reduce the observed shot noise, as we sample more (albeit in a biased way) from the existing galaxies. However, galaxies do not sample the matter distribution uniformly – they reside within haloes. Simply observing more galaxies within haloes does not equate to uniformly sampling the underlying matter distribution. Instead, haloes, which host galaxies, are the entities that sample the large-scale matter distribution. Therefore, on scales larger than the size of haloes, the shot noise is dependent on the number density of haloes rather than individual galaxies. In the weighted power spectrum, the large-scale shot noise depends on the weights of haloes, while the small-scale shot noise depends on the weights of galaxies.

We seek to test the expressions derived here by comparing to the power spectrum of galaxies extracted from the ILLUSTRIS TNG simulation, in the case that galaxies are weighted

by their SFR. Before we do so, we first describe ILLUSTRISTNG, compare the $H\alpha$ luminosity function it predicts to observations, and investigate the contribution of satellites versus centrals as a function of halo mass.

3 THE STAR FORMATION RATE IN ILLUSTRISTNG GALAXIES

In the previous section, we provided the equations for the power spectrum of galaxies when they are weighted with some weight, W . In the case of LIM, W would be the luminosity of the emission line, which for many emission lines is related to the galaxy’s SFR. Hydrodynamical simulations provide physically motivated values of the SFR. In this section, we briefly introduce the ILLUSTRISTNG simulation that we analyse, and examine the SFRs it predicts. In particular, we show that the simulation yields an $H\alpha$ luminosity function that agrees well with observational data. We also examine how much central and satellite galaxies contribute to the total SFR in individual haloes.

3.1 Details of IllustrisTNG

In this work, we primarily use the TNG300-1 output of the ILLUSTRISTNG hydrodynamical simulation (Springel et al. 2017; Pillepich et al. 2018; Marinacci et al. 2018; Naiman et al. 2018; Nelson et al. 2019). TNG300-1 (hereafter TNG) is performed in a cubic volume with comoving side length of 205 cMpc h^{-1} at a dark matter resolution of $m_{DM} \sim 3.98 \times 10^7 M_{\odot} h^{-1}$, and gas resolution of $m_{gas} \sim 7.44 \times 10^6 M_{\odot} h^{-1}$. TNG uses the AREPO moving mesh code (Springel 2010) to solve for gravity and magneto-hydrodynamics. The simulation includes detailed recipes for the subgrid aspects of galaxy formation: gas cooling and photo-heating, star formation, stellar evolution, black hole seeding and growth, and the feedback from stars and accreting black holes (see Weinberger et al. 2017 and Pillepich et al. 2018 for details). Cosmological parameters are taken from PLANCK15 (Ade et al. 2016).

Dark matter haloes are identified from the dark matter particle distribution using the friends-of-friends (FOF) algorithm with the usual value of the linking length ($b = 0.2$) (Davis et al. 1985). Substructures within FOF haloes are identified by the SUBFIND algorithm (Springel et al. 2001), which works as follows: the local density for each particle within a halo is estimated, and density peaks are identified. Particles are assigned to density peaks in order of decreasing density. An unbinding procedure is applied, where unbound particles are removed to identify self-bound substructures. If the number of particles remaining after the unbinding procedure is greater than a predefined threshold number (20), they are labelled as constituting a ‘subhalo’. An FOF halo may contain many subhaloes, each of which contains either zero or one galaxy, consisting of stars, gas and black holes. The subhalo at the minimum of the gravitational potential of the FOF halo is called the central subhalo (identified using the `GroupFirstSub` field in the TNG database²), and all remaining subhaloes are satellite subhaloes, regardless of whether or not they are within the virial radius of the main halo.

A central subhalo can host a central galaxy and a satellite subhalo can host a satellite galaxy. Categorising galaxies as central or satellite is not consistent across simulations; it is also challenging in observations, particularly as the dark matter halo is not directly observed. Nevertheless, the definition used in TNG offers a useful guide for the approximate effect of satellite galaxies.

We quote the database value of `Group_M_TopHat200` for the mass of a halo, and refer to it as its virial mass (M_{vir}). The mean density within a sphere that encloses this mass is Δ_c times the critical density, where the dimensionless number Δ_c follows from the solution of the collapse of a spherical top-hat perturbation. The fitting formula provided by Bryan & Norman (1998) is used to evaluate Δ_c . We further use the database entry `SubhaloSFR` for the SFRs of the galaxies, and `GroupSFR` for the total SFR of the halo (i.e. the sum of the SFRs of the central and satellite galaxies belonging to the same halo). We do not apply any aperture correction, since all SFR should be detected in LIM. Substructures with database label `SubhaloFlag=0` are probably not of cosmological origin, but instead part of a larger galaxy: they are usually ignored when using the database³. However, the LIM luminosity of a voxel will detect all SFR present in that voxel, therefore we also include structures with `SubhaloFlag=0`. Excluding such subhaloes at $z = 1.5$ decreases the SFR density by 4 per cent and the amplitude of the LIM power spectrum by 5 per cent.

We focus mostly on $z \sim 1.5$ with $H\alpha$ LIM surveys such as SPHEREx (Doré et al. 2018) in mind. This redshift will also be observed in CO (SPT-SLIM, Karkare et al. 2022), and [CII] (TIM, Vieira et al. 2020). We briefly show results for other redshifts as well for completeness.

The results we obtain in this study could be dependent on the galaxy formation model adopted in the hydrodynamical simulation, therefore we also compare to the EAGLE simulation (Schaye et al. 2015; Crain et al. 2015). The identification of EAGLE galaxies is also based on SUBFIND, and we use the database described by McAlpine et al. (2016).

3.2 SFR-luminosity relation

The luminosity of many observed emission lines is proportional to the galaxy’s SFR. Examples include CO, which is emitted by the cold molecular gas from which stars form, and $H\alpha$ and O III, which are emitted in star-forming regions (e.g. Bernal & Kovetz 2022). It is common to adopt a linear relationship between the line flux and the SFR, possibly after applying a correction for absorption (by dust and/or gas). This is most appropriate for $H\alpha$, as its emission is due to the recombination of $H II$ in regions photoionised by ultraviolet photons emitted by young, massive stars. Other lines may be less direct tracers of star formation and more affected by metallicity or other environmental factors.

We model the intrinsic $H\alpha$ luminosity using

$$\frac{L_{\alpha}}{\text{erg s}^{-1}} = K \frac{\text{SFR}}{M_{\odot} \text{ yr}^{-1}}, \quad (33)$$

where $K = 2.0 \times 10^{41}$ (Kennicutt 1998) with a ~ 0.63 factor conversion (Madau & Dickinson 2014) from the Salpeter

² [Link to the ILLUSTRISTNG database](#)

³ D. Nelson, private communication.

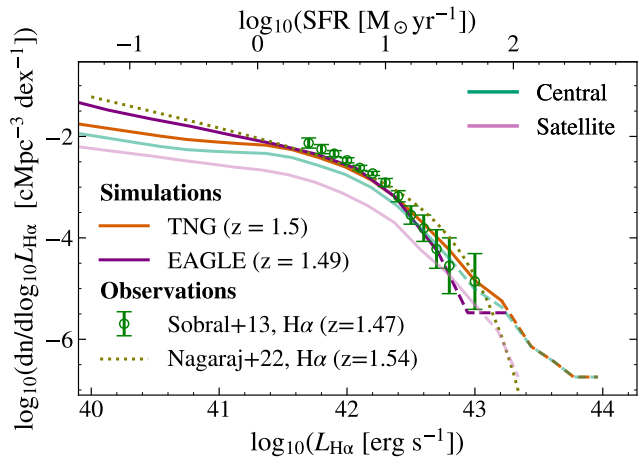


Figure 5. $H\alpha$ luminosity functions (LFs) at redshift $z \sim 1.5$. The *solid lines* correspond to LFs computed from the SFR in the simulations after applying a dust correction ($A_{H\alpha} = 1$, see Eq. (34)). *Orange lines* correspond to TNG at $z = 1.5$ and *purple lines* correspond to EAGLE at $z = 1.49$; lines are *dashed* when there are fewer than 10 haloes in a luminosity bin. The *light green line* and the *light violet line* show the TNG LFs for central and satellite galaxies only. The *open circles* are the observed LF from the HiZELS survey at $z = 1.47$ (Sobral et al. 2013). The *dotted line* is the fit for the observed LF from the 3D-HST survey (Nagaraj et al. 2023). Both simulations generally agree well with each other and with the observations.

(1955) stellar initial mass function (IMF) assumed by Kennicutt (1998) to the more recent Chabrier (2003) IMF). We account for absorption by dust in the galaxy’s interstellar medium (ISM) by reducing the intrinsic $H\alpha$ luminosity to

$$L_{\alpha}^{\text{dust}} = 10^{-A/2.5} L_{\alpha}^{\text{no dust}}, \quad (34)$$

setting $A = 1$, following Garn et al. (2010); Sobral et al. (2012).

In Fig. 5, we compare the $H\alpha$ luminosity function (LF) computed using Eq. (34) from TNG and EAGLE with each other, and with the observations from HiZELS (Sobral et al. 2013) and 3D-HST (Nagaraj et al. 2023). There is generally good agreement between both simulations and the observational data. At the faint end not probed by the observations, the TNG LF is lower than the one from EAGLE. This difference may be a consequence of the lower resolution of TNG. Indeed, fig. 11 in Hirschmann et al. (2023) shows that the LF of the 300 Mpc TNG simulation falls below the LF of the higher resolution simulations of the ILLUSTRISTNG project. The contributions from centrals and satellites are shown separately in Fig. 5 (light green and light purple lines): 30 per cent of the LF is due to satellites for $\log L_{H\alpha} \gtrsim 41.5$.

The good agreement between the simulated and observed LF in Fig. 5 provides some confidence that combining Eq. (34) with the SFR from TNG is a good starting point to investigate the LIM power spectrum. In the following subsections, we will investigate the contributions from central and satellite galaxies to the SFR- M_{vir} relation, the evolution of the mean cosmic SFR density (CSFRD), as well as the distribution of the SFR inside haloes.

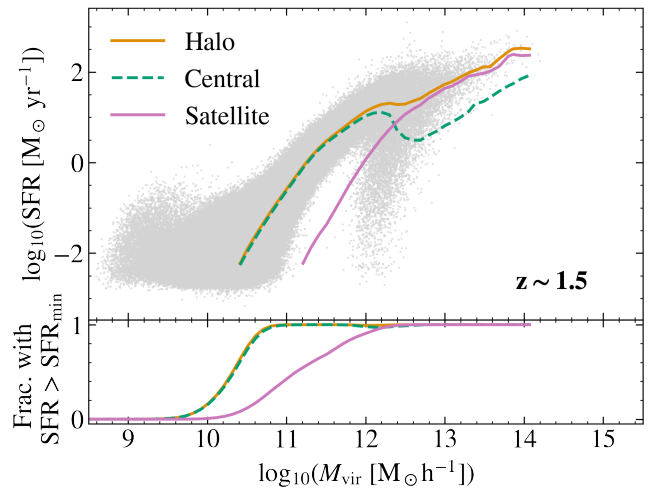


Figure 6. *Upper panel:* SFR- M_{vir} relation of TNG haloes at redshift $z = 1.5$. The *dashed green line* is the median SFR of the central galaxy only, the *solid violet* is the median of the sum of the SFRs of all satellites in a halo, and the *solid orange* is the sum of these two contributions (i.e. the halo SFR). The *grey dots* are the halo SFRs of individual haloes. *Lower panel:* Fraction of haloes for which the SFR is numerically well resolved.

3.3 The contribution of satellite galaxies to the cosmic star formation rate density

We plot the SFR- M_{vir} relation of TNG galaxies at redshift $z = 1.5$ in Fig. 6. On average, the central galaxy contributes more to the halo’s SFR than all satellites combined for $\log M_{\text{vir}} \lesssim 12$ (we will quote halo masses in units of $M_{\odot} h^{-1}$ unless specified otherwise), with satellites dominating the SFR in more massive haloes.

The lower panel of Fig. 6 shows the fraction of simulated haloes with non-zero SFR. Almost 100 per cent of haloes with $\log M_{\text{vir}} \gtrsim 11$ have non-zero SFR, whereas only 20 per cent of halos with $\log M_{\text{vir}} \sim 10$ are star-forming. The fraction of haloes with non-zero SFR in their satellites at $\log M_{\text{vir}} \sim 10$ is ~ 0 per cent, but reaches ~ 100 per cent for $\log M_{\text{vir}} \gtrsim 12$. These values may well depend on the details of the galaxy formation subgrid scheme adopted, but we expect that the general trends will not. In EAGLE, for example, the decrease of the SFR in the central galaxy sets in slightly earlier and is less sudden compared to TNG. The median fraction of star formation in central to satellites also does not reach as low a fraction as in TNG. The different subgrid physics implementations cause differences in the SFR of both central and satellites, as we discuss in more detail in Appendix C1.

To understand the observed LIM power spectrum, it is useful to quantify the extent to which haloes of a given mass contribute to the SFR. Figure 7 shows the contribution to the total SFR from haloes of different masses. Higher mass haloes have higher SFRs on average but then they are rarer than lower mass haloes. As a result, intermediate mass haloes, and in particular those with $\log M_{\text{vir}} \sim 12$ contribute most as they are abundant and have high SFR. The central galaxy dominates the SFR in such haloes because such haloes rarely have highly star-forming satellites. At $\log M_{\text{vir}} \sim 12.5$, satellite galaxies start contributing more to a halo’s SFR than the central. This is both because the SFR of central galaxies be-

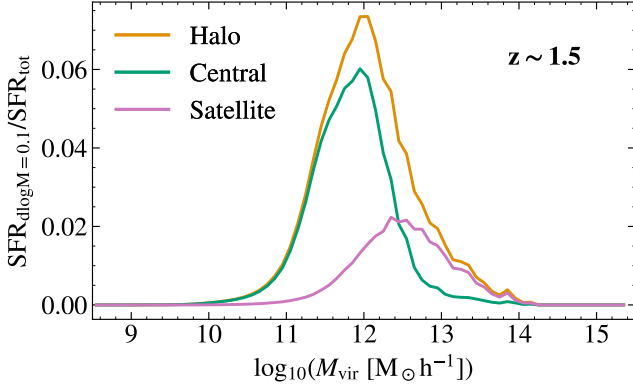


Figure 7. The contribution from different halo masses to the total SFR for haloes (*orange line*), central galaxies (*green line*) and satellite galaxies (*violet line*) in TNG. The amplitudes of the curves is the sum of the SFRs of all haloes in a bin of M_{vir} with bin width $\Delta \log_{10} M_{\text{vir}} = 0.1$, divided by total SFR in the computational volume. The contribution from satellite galaxies becomes larger than that from central galaxies beyond $\log M_{\text{vir}} \sim 12.5$.

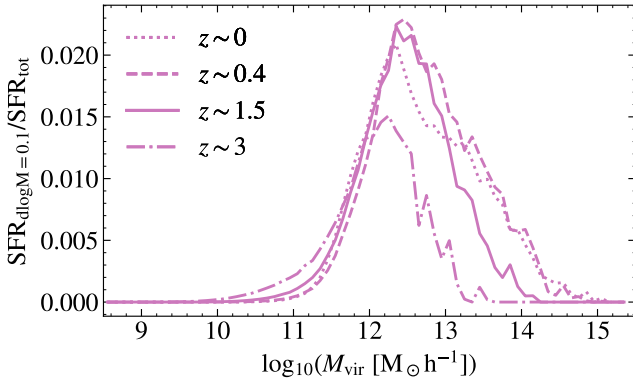


Figure 8. The contribution from different halo masses to the total satellite SFR in TNG at different redshifts as labelled in the panel. Comparing the curves for $z \sim 3$ (*dash-dotted line*), $z \sim 1.5$ (*solid line*) and $z \sim 0.4$ (*dashed line*) shows that the contribution to the SFR from satellite galaxies shifts to more massive haloes at lower redshifts.

comes quenched, and because these haloes typically contain several highly star-forming satellites.

Figure 8 shows the redshift evolution for the contribution of different halo masses to the total satellite SFR. In general, the peak contribution comes from lower halo masses at higher redshifts, as haloes are generally less massive at earlier times. However, the contribution at $z \sim 0$ comes from slightly lower mass haloes than at $z \sim 0.4$, possibly due to satellite SFRs becoming quenched.

Figure 9 shows the CSFRD as a function of redshift (orange lines), as well as the contributions from central (green lines) and satellite galaxies (violet lines) for TNG and EAGLE. At any redshift, the CSFRD is dominated by central galaxies. For TNG, the contribution of satellites increases from ~ 10 per cent at $z \sim 4$ to ~ 30 per cent below $z \sim 1.5$, reaching a maximum of ~ 34 per cent at $z \sim 0.4$. Redshift $z = 4$ is close to the vertical dotted line, which indicates the redshift above which the SFR from haloes with fewer than 100 dark

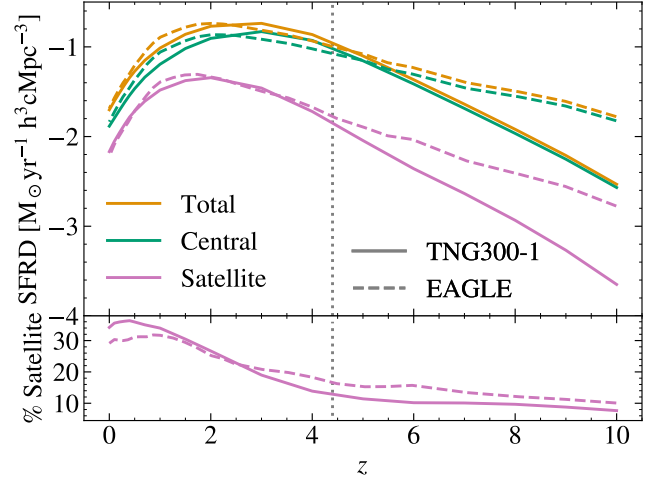


Figure 9. *Upper panel:* CSFRD as a function of redshift, comparing TNG (*solid line*) to EAGLE (*dashed line*). The total SFR density is shown in *orange*, while the contribution from central and satellite galaxies separately are shown in *green* and *violet*. *Lower panel:* Percentage contribution of the SFR due to satellites. The *vertical dotted grey line* indicates the redshift at which the SFR from haloes with fewer than 100 dark matter particles contributes 5% to the total SFR density in TNG. To the right of this line, lack of numerical resolution makes these results less reliable.

matter particles contribute more than 5 per cent to the total SFR in TNG. The lack of numerical resolution may well affect the satellite contribution close to and above this redshift. However, the higher contribution from satellites at low z compared to higher z seems numerically robust, and this trend is seen in both simulations. Below $z \sim 4$, the simulations show good agreement, but at higher redshifts, the SFR in both satellites and centrals is significantly higher in EAGLE compared to TNG. However, it should be noted that both simulations are increasingly affected by numerical resolution at these redshifts.

3.4 The distribution of the SFR inside haloes

How star formation is distributed inside haloes impacts the small-scale LIM power spectrum if haloes are spatially resolved. Figure 10 shows two examples of the distribution of star-forming galaxies in TNG haloes of mass $\log M_{\text{vir}} \sim 12$ and $\log M_{\text{vir}} \sim 13$. Although the total gas is distributed widely, the *star-forming* gas is generally concentrated at the centres of subhaloes. The SFR is not all at the centre of the halo, and some LIM observations have angular resolutions which resolve the distribution of the SFR in sufficiently large haloes (e.g. Keating et al. 2016, 2020). Although not all LIM surveys will be able to resolve haloes, the upcoming SPHEREx will spatially resolve haloes of mass $\log M_{\text{vir}} \sim 12$ at $z \sim 1.5$. The resolution of the survey is indicated by the grey dotted grid in Fig. 10.

4 IMPACT OF SATELLITE GALAXIES ON THE POWER SPECTRUM

In the previous section, we illustrated the contribution of satellite galaxies to the total SFR and how this SFR is spa-

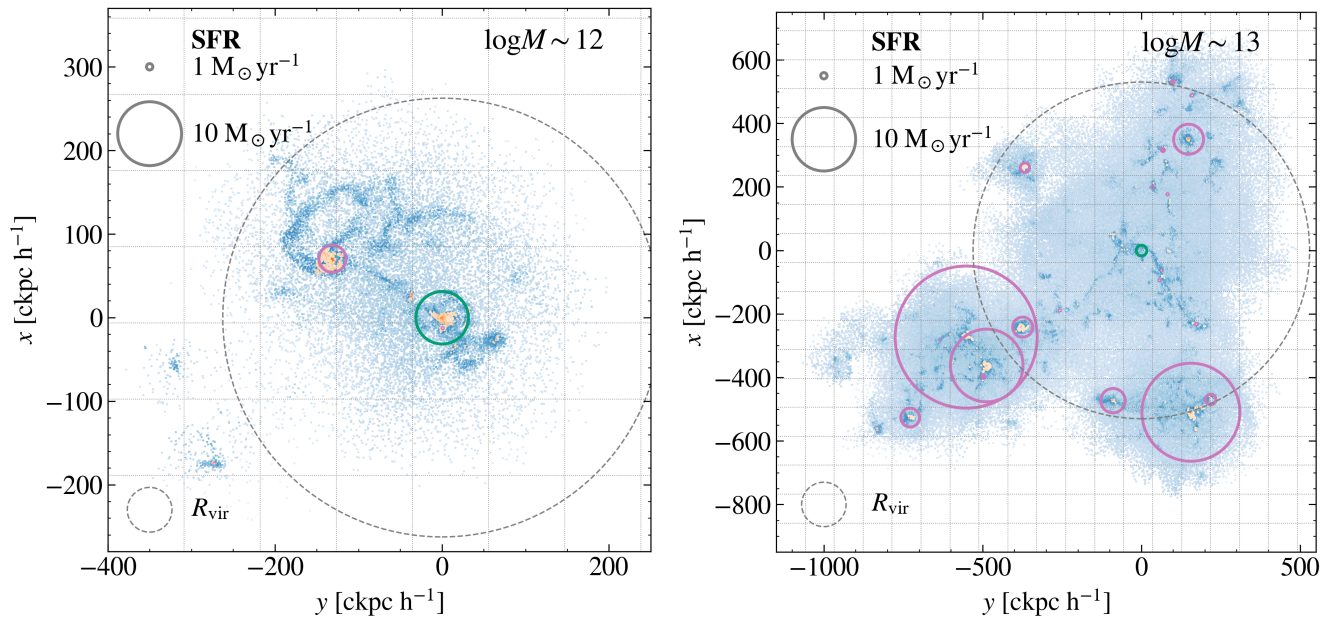


Figure 10. The distribution of star-forming galaxies in TNG haloes. In both panels, the *dashed grey circle* indicates the virial radius of the halo, while galaxies are indicated by a *circle* with a radius proportional to the SFR. The *green circles* correspond to the central galaxy, and *violet circles* correspond to satellite galaxies. The *dotted blue points* are gas particles, and *dotted orange points* are star-forming gas particles. The *left panel* shows a halo with mass $\log M_{\text{vir}} \sim 12$ and total SFR $\sim 13 M_{\odot} \text{yr}^{-1}$; the halo in the *right panel* has $\log M_{\text{vir}} \sim 13$ and SFR $\sim 72 M_{\odot} \text{yr}^{-1}$. (Please notice the difference in linear scale of the panels.) The *light grey dotted grid lines* mark the angular resolution ($6.2''$) for the SPHEREx survey ($\sim 91 \text{ ckpc h}^{-1}$ at $z = 1.5$). Both haloes would be spatially resolved in the data. (These haloes are index 564 and 17776 in the FOF halo catalogue in TNG).

tially distributed inside of their host halo. Their net contribution and their spatial distribution are two ways in which satellites affect the galaxy power spectrum. In this section, we will consider these effects in detail by comparing three different ways of assigning SFRs. Two of the schemes are illustrated in Fig. 2. The ‘galaxy’ scheme is most similar to the real Universe: the SFR of satellites is assigned to their sub-haloes. To test whether the spatial distribution of the satellite SFR matters, we consider the ‘halo’ scheme, in which the SFR of all galaxies in the same halo are summed and placed at the position of the central galaxy. The total SFR of a halo is identical in both schemes. In the third and final case, we examine whether the SFR of satellites matters at all by simply neglecting their contribution to the total SFR altogether. We refer to the power spectrum corresponding to this case as the ‘central’ power spectrum. We show the effect of removing satellite galaxies in Section 4.1 and the effect of how they are spatially distributed inside their host halo in Section 4.2.

We compute the power spectrum using the PYTHON package NBODYKIT (Hand et al. 2019) with PYTHON version 3.6. We assign the SFR of galaxies onto a mesh using the triangular-shaped cloud interpolation scheme with interlacing, adopting cells with size $0.091 \text{ cMpc h}^{-1}$. This cell size corresponds to the angular resolution of SPHEREx ($6.2''$) at $z = 1.5$. See Appendix D for a discussion on how our results depend on the choice of interpolation scheme.

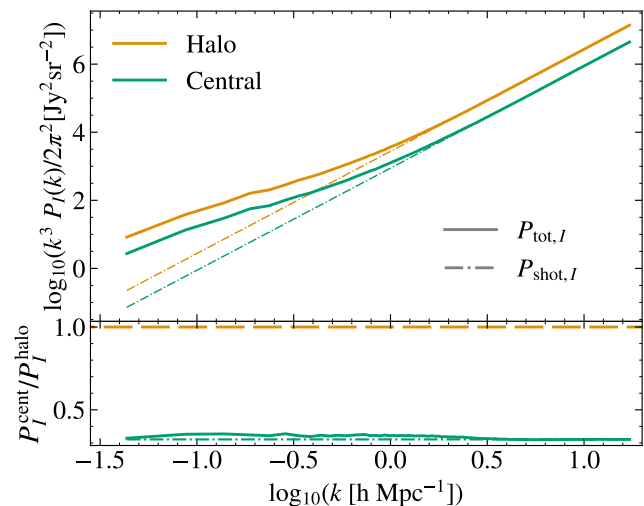


Figure 11. *Upper panel:* Power spectrum of galaxies weighted by their SFR in TNG at redshift $z = 1.5$, scaled in terms of the intensity that would be measured in a LIM survey. The ‘halo’ power spectrum (*orange lines*) assigns the SFR of galaxies to the centre of their host halo, while the ‘central’ power spectrum neglects satellites. *Solid lines* are the total power spectrum, *dash-dotted lines* are the shot noise contribution. *Lower panel:* The ratio of the central over the halo power spectra, for total (*solid lines*) and shot-noise (*dash-dotted lines*). The ‘central’ power spectrum is less than ~ 40 per cent of the ‘halo’ power spectrum, and the suppression is similar for the shot-noise contribution. We show results for H α but these results should also hold for other lines.

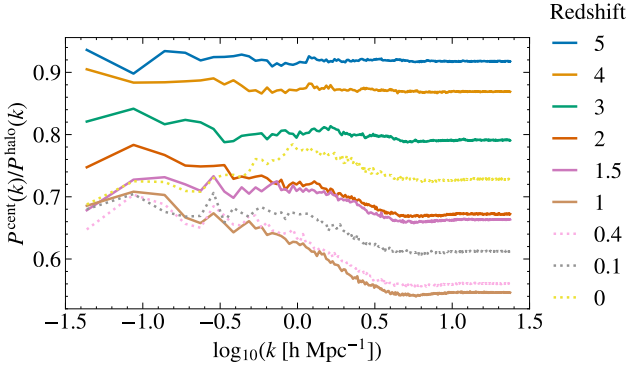


Figure 12. The ratio of the central power spectra to halo power spectra, with both power spectra divided by their respective specific mean intensities. It is in effect the ratio $(b_{\text{cent}}(k)/b_{\text{halo}}(k))^2$. This is shown for different redshifts, with line colours and styles indicated by the legend. The effect of satellites increases with decreasing redshift down to $z \sim 0.4$. *Dotted lines* are used for $z \sim 0.4, 0.1$ and 0 to emphasise the reversal of the trend from higher z . The bias of central galaxies only is lower than that of the haloes when satellites are included.

4.1 Impact of star formation in satellites on the power spectrum

We compute the power spectrum with galaxies weighted by their SFR, in two ways: (i) the ‘central’ power spectrum ($P_{\text{cent},I}$), which only accounts for central galaxies, and (ii) the ‘halo’ power spectrum ($P_{\text{halo},I}$, right panel of Fig. 2). The latter is computed after adding the SFR of satellites to the central galaxy. The total number density of sources is the same but the total SFR is higher in the halo case.

The lower panel of Fig. 11 shows the ratio of the central power spectrum to the halo power spectrum, while the upper panel shows the absolute power spectra. The power spectra have not been divided by the mean intensity. We find that the amplitude of the central power spectrum is ~ 35 per cent of that of the halo power spectrum, indicating that removing satellite galaxies results in a significant underestimate of the power spectrum.

The LIM power spectrum can be written as $P(k) = \bar{I}^2 b(k)^2 P_m(k)$, showing that both the specific mean intensity and the bias affect the power spectrum. The specific mean intensity is set by the CSFRD. In Fig. 9, we showed that satellite galaxies contribute $\sim 30\%$ to the CSFRD at $z = 1.5$. This scales with the specific mean intensity, \bar{I} , by a constant factor. The intensity power spectrum is proportional to the mean intensity squared, so the difference due to the contribution from the SFR of satellites would cause $P_{\text{cent},I}$ to be ~ 50 per cent of $P_{\text{halo},I}$, but we find $P_{\text{cent},I}$ to be even lower than this. This suggests that the inclusion of satellite galaxies also affects the bias, $b(k)$.

Figure 12 shows the ratio of the central power spectrum to the halo power spectrum but with the power spectra divided by the square of their respective specific mean intensities, such that the ratio corresponds to $(b_{\text{cent}}(k)/b_{\text{halo}}(k))^2$. The evolution with redshift is also displayed. The violet line shows that even when we consider the intensity-divided power spectrum, P_{cent} is ~ 70 per cent of P_{halo} at $z = 1.5$. The reason for the difference is that satellite galaxies tend to reside in higher mass haloes. Such haloes are more highly biased (Tin-

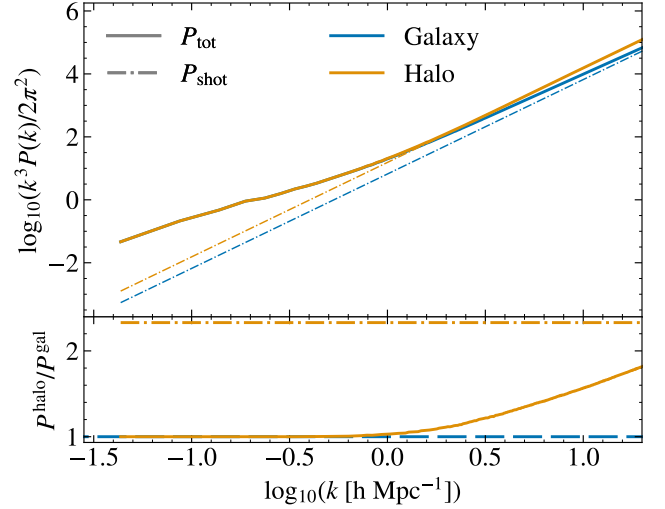


Figure 13. The halo power spectrum (orange) compared with the galaxy power spectrum (blue). The solid line represents the total power spectrum and the dash-dotted line represents the Poisson shot noise power spectrum. The bottom panel shows the ratio of the halo power spectrum relative to the galaxy power spectrum, respectively for the total and shot noise power spectrum.

ker et al. 2010). When satellite galaxies are included, higher mass haloes have higher weight, causing the overall bias to be higher in the ‘halo’ case.

The contribution of satellite galaxies to the CSFRD increases with decreasing redshift, at least until $z \sim 0.4$, as we showed in the previous section. As a consequence, satellites will also contribute more to the power spectrum at lower z .

The amplitude of the power spectrum is set by the shot noise on small scales. Although the number density of galaxies is the same in the ‘halo’ and ‘central’ case, the shot noise contribution is different. Indeed, the shot noise scales with $\text{Var}(L)/\langle L \rangle^2$, where $\text{Var}(L)$ is the variance in luminosity, as we demonstrated in Eq. (12). Accounting for satellites in TNG increases the variance more than the square of the mean, resulting in a higher shot noise in the ‘halo’ case.

4.2 Impact of the spatial distribution of satellites on the power spectrum

In the previous section, we have only considered the case where all the SFR is at the centre of haloes, yielding what we refer to as the halo power spectrum. This would be the power spectrum obtained from some of the fast simulation codes (e.g., Monaco et al. 2002), which only have the mass and position of the FOF haloes and do not track the satellite subhaloes, in exchange for speed. However, as we have seen in Fig. 10, the SFR is not all at the centre, and the resolution of surveys like SPHEREx ($6.2''$) would be able to resolve the spatial distribution of the SFR in a halo.

In this subsection, we provide a comparison of the halo power spectrum with the galaxy power spectrum, which more closely reflects the observed power spectrum. This helps us understand the contributions to the power spectrum and how the power spectrum computed from haloes only would differ from the observed power spectrum.

Figure 13 shows the halo and galaxy power spectra. They

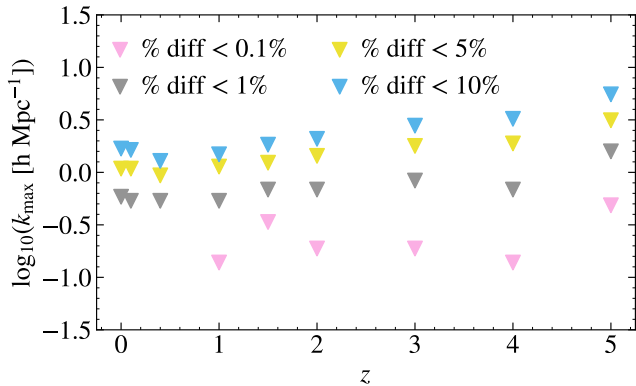


Figure 14. The wavenumber up to which the galaxy and halo power spectra agree to within 0.1% (pink), 1% (grey), 5% (green) and 10% (blue) for several redshifts. The 0.01% values for $z < 1$ are not shown as the variation in the ratio is larger than 0.1% (the percentage error does not clearly stay below 0.1%).

agree on large scales, but on small scales, the halo power spectrum tends to the *halo* Poisson shot noise, $P_{\text{shot}}^{\text{halo}}$, whereas the galaxy power spectrum tends to the galaxy Poisson shot noise, $P_{\text{shot}}^{\text{gal}}$. The halo Poisson shot noise is higher than that of galaxies as there are fewer haloes than there are galaxies, and the variance of luminosities is larger (see Eq. (12)).

The difference between the halo and galaxy power spectra becomes non-negligible when $U(k) \neq 1$ (see Eq. (1)). Figure 14 shows, for several redshifts, the k values up to which the halo and galaxy power spectra agree to within a certain percentage. At lower redshifts, the sizes of haloes are generally larger, so the wavenumbers up to which the power spectra agree is smaller ($U(k) = 1$ beyond the size of the largest halo). We find that a model which does not distribute the satellite galaxies is sufficient to reproduce the large-scale power spectrum to within 1 per cent on scales $\log k \lesssim -0.3$ for $z \lesssim 5$ (we will quote wavenumbers, k , in units of $h \text{ Mpc}^{-1}$ unless specified otherwise). The findings are similar when comparing the galaxy and halo power spectra computed for the EAGLE simulation.

5 A MODEL FOR THE GALAXY POWER SPECTRUM

A LIM survey such as that proposed by SPHEREx will sample the galaxy power spectrum from cosmological, nearly linear large scales, all the way down to smaller scales comparable to or even smaller than those of haloes. Here we present details of a model that captures this full range of scales. We already showed some results of this model in Section 2 (Eq. (1)). In Fig. 1, we plotted the components of the model against the corresponding components in TNG, and showed that our model could reproduce the TNG power spectrum to within 15 per cent. The model has fitting parameters which all have a clear physical interpretation.

The model is motivated by the ‘halo model’ (Cooray & Sheth 2002) for the matter power spectrum, and consists of a 2-halo term – arising from the clustering of haloes – and a 1-halo term – arising from the distribution of galaxies in a given halo. In Section 5.1, we provide a fit for the 2-halo term

which accounts for halo exclusion and non-linear halo clustering outside the exclusion radius. In Section 5.2, we provide a fit for the 1-halo term, which accounts for the different origins of shot noise on large and small scales, and is based on how galaxies are distributed inside a halo. Finally, in Section 5.3, we summarise the parameters of the model.

5.1 Fitting the 2-halo term – including nonlinearity and halo exclusion

The 2-halo term imprints the clustering of haloes on the galaxy power spectrum. We compute this term in the simulations by Fourier transforming the density field of haloes, where each halo is a point object with a weight equal to the total SFR of all its galaxies. The 2-halo term is the power spectrum of the weighted halo density field after subtracting the halo shot noise term (Eq. (13)). As before, we use NBODYKIT (Hand et al. 2019) to perform this calculation, accounting for aliasing. The 2-halo power spectrum for TNG is plotted as open orange circles in Fig. 1.

Note that the 2-halo term in the galaxy power spectrum differs slightly from that in the halo power spectrum on scales smaller than the size of haloes (where $\hat{v}_h^{(s)}(\mathbf{k}) \neq 1$ in Eq. (28)). The distances between galaxies in a pair of haloes are not identical and will be noticeable on these scales. Nevertheless, we still use this 2-halo term as an approximation to the one in the galaxy power spectrum. In Section 4.2, we showed that the galaxy power spectrum deviates from the halo power spectrum for $\log k \gtrsim -0.5$. This marks the scale where $\hat{v}_h^{(s)}(\mathbf{k}) < 1$ for some haloes, in which case the 2-halo term in the galaxy power spectrum may be smaller than that in the halo power spectrum, and thus the 1-halo term would be larger than proposed (since the 1-halo term is derived by subtracting the 2-halo term of the halo power spectrum). At $\log k \sim -0.5$, only the largest haloes will have $\hat{v}_h^{(s)}(\mathbf{k}) < 1$, therefore the difference between the galaxy and halo 2-halo term will be small, with the difference increasing at smaller scales where more haloes will have $\hat{v}_h^{(s)}(\mathbf{k}) < 1$.

We expect the 2-halo term to be a biased version of the matter power spectrum on scales much larger than the radii of haloes. Nonlinearity will start to play a role on scales comparable to those radii. Finally, on scales smaller than the radii of the largest haloes, we expect that halo exclusion will play an increasingly important role.

Halo exclusion imprints a feature in the correlation function $\xi(r)$: if all haloes had the same size, the correlation function $\xi(r) = -1$ for $r < d$ (where d is the minimum distance between a pair of haloes before they overlap, i.e. d is twice the halo’s radius; see, e.g., Baldauf et al. 2013). Since they do not all have the same size, we expect this step-like feature in ξ to be smeared out. Therefore, we need to find the probability distribution of exclusion distances, PDF(d). Baldauf et al. (2013) propose a lognormal distribution,

$$\text{PDF}(d) = \frac{1}{(\ln 10)d\sigma\sqrt{2\pi}} \exp\left[-\frac{(\log_{10}(d/d_0))^2}{2\sigma^2}\right], \quad (35)$$

with parameters $\log_{10} d_0$ (the logarithmic mean value of d) and σ (the logarithmic scatter around the mean). The probability of finding a pair of haloes whose separation is larger

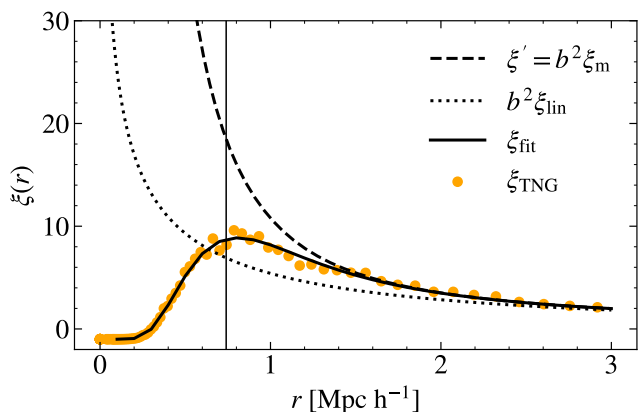


Figure 15. The SFR-weighted halo correlation function at $z = 1.5$. The correlation function measured from TNG is shown by orange dots, and the fit discussed in the text is plotted as a solid black line. The fit is described by three parameters: a constant bias, b , relative to the non-linear correlation function, and two parameters that characterise halo exclusion. This fit captures the non-linear enhancement outside the exclusion radius as well as the decrease at small radii caused by halo exclusion. The dashed black line is b^2 times the non-linear correlation function, and the dotted black line is b^2 times the linear correlation function. The vertical solid line marks the mean exclusion radius.

than some distance r is then

$$f(r) = 1 - \frac{1}{2} \left(1 + \operatorname{erf} \left[\frac{\log_{10}(r/d_0)}{\sqrt{2}\sigma} \right] \right). \quad (36)$$

This is the function that appears in Eq. (19).

We have measured the distribution of halo separations in TNG directly⁴ for haloes in the range $\log M_{\text{vir}} = 12 - 12.5$. The measured probability distribution of halo separations is described well by the lognormal model of Eq. (35).

Before we can compute the halo power spectrum by Fourier transforming ξ , we need to compute the correlation function on scales comparable to or even smaller than the typical halo radius – indeed, some smaller haloes in the lognormal distribution can be closer together than larger haloes. We referred to this extrapolated correlation function as $\xi'(r)$ in Eq. (19) (see Section 2.3.1). We find that the ratio of $\xi'(r)$ to the linear matter correlation function depends on r : linear bias is not a good description for halo bias. However, we find that, the ratio of $\xi'(r)$ to the *non-linear* matter correlation function is approximately constant, at least at $z \sim 1.5$. This finding agrees with the results of Sheth & Tormen (1999), who also found that the non-linear bias of haloes is approximately constant (for $z \sim 2$ in their case). At both higher and lower z , the non-linear bias becomes scale-dependent, as also shown by Sheth & Tormen (1999) (their fig. 1). A more detailed investigation of the scale-dependence of bias is beyond the scope of the present study but, in principle, the same exclusion formula could be combined with a better model for scale-dependent bias at other redshifts.

We use Eq. (19) as a fitting function for the SFR-weighted

correlation function, with $f(r)$ given by Eq. (36). We compute the non-linear matter correlation function, ξ_m , with the HALOFIT model⁵ of Takahashi et al. (2012). The extrapolated correlation function $\xi'(r)$ is then taken to be $b^2\xi_m$. The three parameters of ξ are d_0 and σ , which characterise exclusion (see Eq. (36)), and the bias parameter b . Fitting to the halo correlation function in TNG, we obtain best-fitting values of $d_0 = 0.74 \text{ cMpc h}^{-1}$, $\sigma = 0.17 \text{ dex}$ and $b = 2.0$.

In Fig. 15, the fit (solid black line) is compared to the halo correlation function measured in TNG (orange dots). On scales $r \geq 2 \text{ cMpc h}^{-1}$, the TNG correlation function is well approximated by b^2 times the linear (dotted line) or non-linear correlation function (dashed line). On smaller scales, $1 \leq r/\text{cMpc h}^{-1} \leq 2$, nonlinearity increases the TNG correlation function above the biased linear correlation function: this increase is captured well by b^2 times the non-linear correlation function. On even smaller scales, halo exclusion is detected in TNG, and the rapid decrease in amplitude of the halo correlation function to smaller scales is captured well by our model.

We note that the halo exclusion multiplier $f(r) \leq 1$ for all r , hence $\xi(r) \leq \xi'(r)$ for all r . Therefore, the amplitude of $\xi'(r)$ needs to be higher than that of the halo correlation function at all r . Figure 15 shows that this is not true for the linear correlation function (dotted line) for $r \sim 1 \text{ cMpc h}^{-1}$ – which is why the non-linear correlation function is needed in the definition of ξ .

We Fourier transform the fit to the correlation function to get the model's power spectrum. The halo exclusion feature in the correlation function creates wiggles in the power spectrum (Fig. 16). The figure also shows the scale-dependent bias with respect to the linear and non-linear power spectrum (left and right panel). The model presented here (solid black line) – which uses the non-linear matter power spectrum and takes into account the halo exclusion effect – reproduces the power spectrum measured in TNG (orange dots). We show in Appendix C2 that a similar fit also reproduces the power spectrum measured in EAGLE.

The left panel of Fig. 16 shows that the linear power spectrum multiplied by a constant bias (dotted line) underestimates the TNG 2-halo term on intermediate scales of $\log k \sim 0$. On the other hand, multiplying the non-linear matter power spectrum by a constant bias – without accounting for halo exclusion (dashed line) – overestimates the TNG power spectrum on these scales. Our model does better than a constant bias model as it accounts for both non-linear halo bias and halo exclusion.

When using the non-linear matter power spectrum as $\xi'(r)$, it is important to clarify that this does not represent the halo clustering in the absence of exclusion. Such an interpretation would be incorrect as it includes the 1-halo term. We are simply using it as a tool to reproduce the observed 2-halo term, which includes halo exclusion. By removing the power on scales smaller than the size of haloes due to halo exclusion, we naturally remove the effect of the 1-halo term.

In Fig. 1, the largest difference between TNG and the model is on the largest scales – this is where the impact of sample variance is greatest. To estimate the impact of sample

⁴ We estimate the FOF radius of haloes by multiplying the virial radius by $(M_{\text{FOF}}/M_{\text{vir}})^{1/3}$. Then, we find the probability distribution of all pairs of FOF radii.

⁵ We use HALOFIT – rather than measuring the correlation function from TNG directly – purely for computational ease.

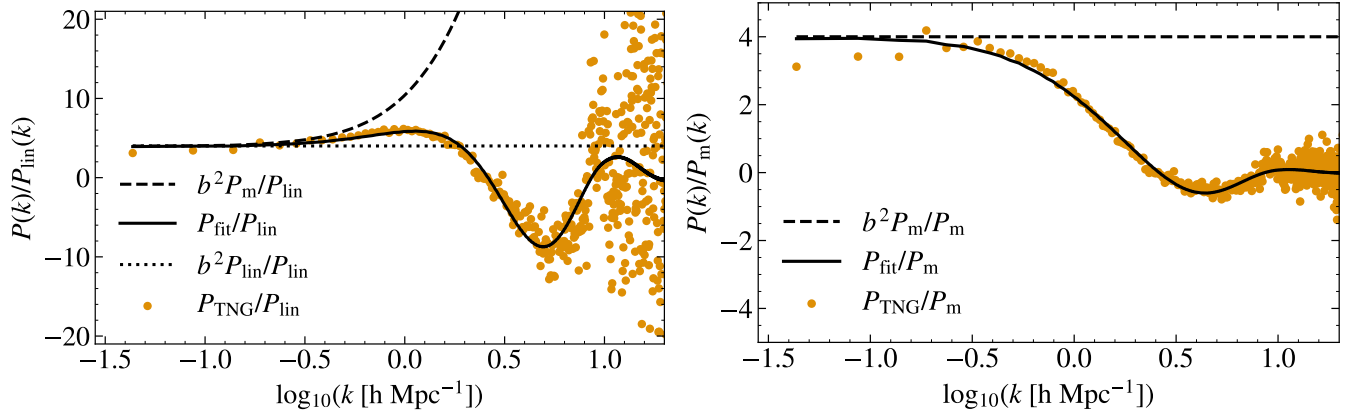


Figure 16. The impact of halo exclusion and non-linear clustering on the halo power spectrum at $z = 1.5$. *Left panel:* The 2-halo power spectrum of our model (*black line*) compared to the power spectrum measured in TNG (*orange dots*): both power spectra are divided by the linear power spectrum of Eisenstein & Hu (1998). The *dashed black line* is b^2 times the non-linear matter power spectrum divided by the linear power spectrum, where b is the bias. The *dotted line* is the square of the constant bias value we use in our fit. *Right panel:* The *black solid line* is the ratio of the 2-halo power spectrum of our model over the non-linear matter power spectrum. The *orange dots* show the TNG 2-halo term divided by the non-linear power spectrum. Our fit to the 2-halo term – which includes a bias with respect to the non-linear matter spectrum and a correction for halo exclusion – reproduces the power spectrum measured in TNG.

variance, we compute the TNG matter power spectrum at the start of the simulation ($z \sim 127$), where the power spectrum is expected to be linear. We then multiply the result by a scaling factor – in this case, the power spectrum at $z = 1.5$ agrees with the scaled power spectrum for $\log k \lesssim -0.8$, indicating the scale above which the power spectrum is still linear. This suggests that the error on scales $\log k \lesssim -0.8$ is due to sample variance.

In summary, the 2-halo contribution to the TNG power spectrum is not fit well by multiplying the linear power spectrum with a constant bias: this fails to capture the shape of the power spectrum on scales comparable to that of haloes ($\log k \sim 0$) and (unsurprisingly) is even worse at smaller scales. Our model – which uses a constant bias relative to the non-linear power spectrum and accounts for halo exclusion – fits the TNG 2-halo term on all scales at $z \sim 1.5$. We turn to the 1-halo term next.

5.2 The 1-halo term – halo profile and shot noise

We compute the 1-halo term of a simulation power spectrum by subtracting the 2-halo term of the halo power spectrum from the total galaxy power spectrum (Eq. (1)). The result is plotted as open red circles in Fig. 1 for the TNG simulation. Whereas the 2-halo term results from the clustering of galaxies in different haloes, the 1-halo term arises from correlations of galaxies within the same halo, including with themselves.

Equation (1) shows that the 1-halo term combines three contributions: (i) shot noise from haloes, (ii) shot noise from galaxies, and (iii) a term that reflects the distribution of galaxies in haloes. Determining these contributions can help constrain the galaxy formation model. Understanding the 1-halo term is also important on large scales, where shot noise contributes to the measured power spectrum.

In Section 5.2.1, we discuss the amplitude of the 1-halo term, which is set by galaxy shot noise on small scales and halo shot noise on large scales. In Section 5.2.2, we discuss the

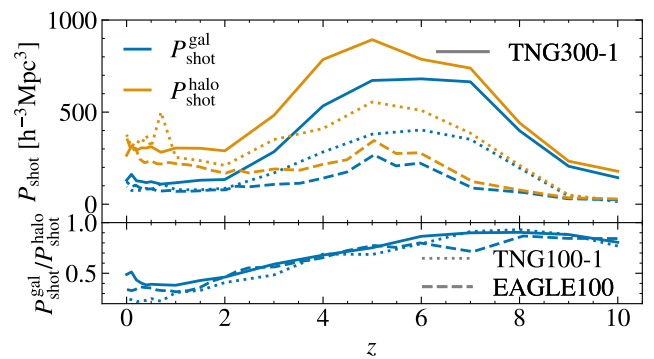


Figure 17. Amplitude of the shot noise term as a function of redshift. The galaxy shot noise, $P_{\text{shot}}^{\text{gal}}$, is plotted in *blue*, and the halo shot noise, $P_{\text{shot}}^{\text{halo}}$, in *orange*. Results for TNG (ILLUSTRISTNG300-1) are shown by *solid lines*, for TNG100-1 as *dotted lines*, and for EAGLE as *dashed lines*. The *upper panel* shows the amplitude of the shot noise terms, and the *lower panel* shows the ratio $P_{\text{shot}}^{\text{gal}}/P_{\text{shot}}^{\text{halo}}$. For all simulations, $P_{\text{shot}}^{\text{gal}}$ increases with decreasing redshift down to $z \sim 5$, and then decreases again. There are significant differences in amplitude between TNG300-1 and TNG100-1, presumably due to differences in numerical resolution. TNG100-1 and EAGLE have similar numerical resolution, yet there are still noticeable differences in the amplitude of the shot noise between the two simulations. At higher redshifts, where the contribution of satellites to the CSFRD is smaller, the difference between the galaxy and halo shot noise is smaller for all simulations.

shape of the 1-halo term, which depends on the distribution of luminosity in haloes.

5.2.1 Galaxy and halo shot noise contributions to the 1-halo term

We compute the shot noise using Eq. (11), summing over all simulated galaxies for the galaxy shot noise term, $P_{\text{shot}}^{\text{gal}}$, and over all haloes, with weight equal to the sum of their galaxies’

SFRs, for the halo shot noise term, $P_{\text{shot}}^{\text{halo}}$. By construction, these numbers are independent of scale. They are plotted as a function of redshift in the upper panel of Fig. 17. With increasing redshift, increasingly fewer haloes have highly star-forming satellites, and the values of the two shot noise terms becomes similar. The ratio of the two terms are shown in the lower panel of Fig. 17. The galaxy shot noise is $\sim 50\%$ of the halo shot noise for $z \lesssim 2$, rising to 75% at $z \sim 4$.

We also show the shot noise computed using the TNG100-1 simulation (dotted lines) and the EAGLE simulation (dashed lines) to show the effect of resolution and galaxy formation model; both have a simulation box of around 100 cMpc and comparable numerical resolution. Both of these are higher in resolution than the TNG300-1 simulation. The shot noise computed in the TNG100-1 simulation is lower than in the TNG300-1 simulation, both because star formation is better resolved, resulting in a higher volume density of star-forming galaxies, and because the SFR of a galaxy tends to be higher at higher resolution in the ILLUSTRISTNG model. Indeed, while the hydrodynamical simulations have well-motivated physical processes, the simulations are not yet fully converged in resolution (see e.g. Pillepich et al. 2018). In particular, resolution affects the SFR (see fig. 11 of Hirschmann et al. 2023) and hence the amplitude of the shot noise term. The shot noise computed from the EAGLE simulation is even lower than the one computed from TNG100-1. Although the variance of the SFR is higher in the EAGLE simulation, the mean is also higher, resulting in a lower shot noise in EAGLE.

The surprisingly large differences between simulations with different resolutions (TNG300-1 versus TNG100-1), or between different implementations of galaxy formation (TNG100-1 versus EAGLE) sound a note of caution when using simulations to estimate the shot noise term in an observed data set ($P_{\text{shot}}^{\text{halo}}$ cannot easily be measured in the data since haloes are not observable). Nevertheless, the qualitative trends are relatively independent of resolution: there is a difference between galaxy and halo shot noise at all redshifts, with the difference becoming less significant with increasing z .

We stress that $P_{\text{shot}}^{\text{gal}}$ – which might conceivably be measured from the observed small-scale galaxy power spectrum – is not the correct shot noise to be used on large scales. If one subtracts $P_{\text{shot}}^{\text{gal}}$ rather than $P_{\text{shot}}^{\text{halo}}$ from the galaxy power spectrum, then the 2-halo term, and therefore the bias, will be estimated incorrectly. Figure 18 illustrates the errors incurred if one subtracts the wrong shot noise. The orange dotted line shows the halo power spectrum with the halo shot noise subtracted. This is our reference for the correct 2-halo term on large scales (where $U(k) = 1$; see Eq. 1).

Several common assumptions are made when discussing shot noise, some of which are illustrated in Fig. 18. The first common assumption is that the galaxy shot noise is independent of scale. The blue dotted line shows the case where only the galaxy shot noise is subtracted from the galaxy power spectrum. If we assume that subtracting the galaxy shot noise gives the 2-halo term then it is overestimated by more than 1 per cent on large scales. Another common assumption is that the 1-halo term tends to the halo shot noise on large scales and that the galaxy shot noise is constant on all scales. In this case, subtracting the sum of the galaxy shot noise and the halo shot noise should give the 2-halo term. However, the grey dotted line shows that doing this underestimates the

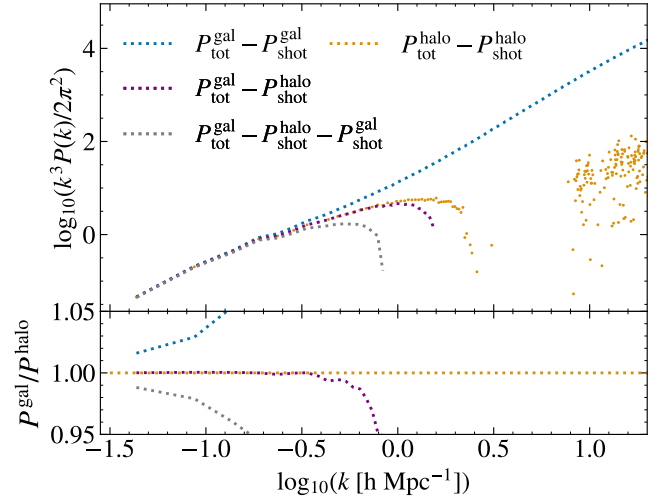


Figure 18. Galaxy power spectrum of TNG at $z = 1.5$, $P_{\text{tot}}^{\text{gal}}$, minus various choices for the shot noise. The shot noise subtracted is that of galaxies (blue dotted), haloes (purple dotted), and both galaxies and haloes (grey dotted lines). The yellow dotted line is the halo power spectrum with the halo shot noise subtracted (2-halo term of halo power spectrum). The top panel shows the dimensionless power spectrum, plotted to reduce the dynamic range. The lower panel shows the shot noise-subtracted power spectra divided by the 2-halo term derived from the halo power spectrum (yellow dotted line). As argued in the text, the halo shot noise is the correct term to subtract: in this case, the galaxy power spectrum with the halo shot noise subtracted is equal to the 2-halo term derived from the halo power spectrum for $\log k \lesssim -0.5$. Beyond this, the distribution of galaxies within haloes affects the galaxy power spectrum. Subtracting the galaxy shot noise leads to an overestimate of the 2-halo term of 2 per cent on the largest scale, with the error increasing towards smaller scales. Subtracting both the galaxy and halo shot noise term leads to an underestimate of the 2-halo term.

2-halo term by more than 1 per cent. Subtracting only the halo shot noise allows us to reproduce the 2-halo term to within 0.01% for $\log k \lesssim -0.5$, confirming that the halo shot noise is the correct shot noise on large scales. The shot noise-subtracted galaxy and halo power spectra start to deviate for k sufficiently large such that $U(k)$ – the Fourier transform of the halo profile – deviates significantly from 1. Figure 18 shows that on the largest scales in TNG, shot noise is not negligible and therefore the distinction between the galaxy and halo shot noise must be made in order to estimate the 2-halo term accurately.

While subtracting the correct shot noise term is important to obtain the correct 2-halo term on all – including large – scales, it is also worth investigating what information can be obtained from the term itself. By measuring the small scales where the galaxy Poisson shot noise is dominant, we can obtain information about the luminosities of galaxies (Eq. (12)), providing a constraint on their luminosity function. We only have the total power spectrum from observations, therefore to determine if the galaxy shot noise is dominant, one should check that the slope of the power spectrum is constant on those scales. In Fig. 1, we plotted the power spectra to half the Nyquist frequency of the SPHEREx pixel length at $z = 1.5$. At these scales, the galaxy Poisson shot noise is not yet dominant.

Similarly, the halo shot noise could, in theory, provide a

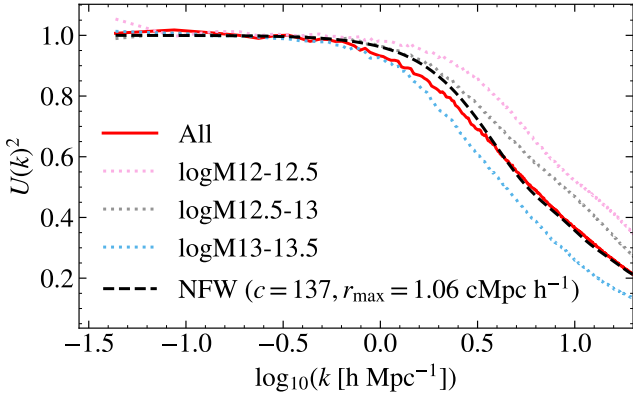


Figure 19. The luminosity-weighted average of the square of the Fourier transform of the luminosity distribution within haloes computed using Eq. (1). The *solid red line* is computed from the power spectrum including all the haloes. The *pink, grey and blue dotted lines* show that computed using power spectra including haloes with mass in the ranges $\log M_{\text{vir}} = 12 - 12.5$, $\log M_{\text{vir}} = 12.5 - 13$ and $\log M_{\text{vir}} = 13 - 13.5$, respectively. The square of the Fourier transform of an NFW profile with parameters $c = 137$, $r_{\text{vir}} = 0.5$ cMpc h^{-1} and $r_{\text{max}} = 1.06$ cMpc h^{-1} is shown by the *dashed black line*. The $U(k)^2$ for the total power spectrum lies between that for $\log M_{\text{vir}} = 12.5 - 13$ and $\log M_{\text{vir}} = 13 - 13.5$.

constraint on the luminosity-weighted abundance of haloes. However, while the galaxy shot noise can be measured on small enough scales, the halo shot noise is always either subdominant or multiplied by $U(k) \neq 1$, and it is therefore not straightforward to extract its value from the observation directly unless one does forward modelling. Nevertheless, the halo shot noise could be considered to be a free parameter which is a constant on scales where the 2-halo term dominates. The value of the halo shot noise is always larger than that of the galaxy shot noise by construction, thus the galaxy shot noise measured on small scales can provide a lower bound.

5.2.2 Inferring the halo profile from the 1-halo term

We demonstrated in Section 2.4.2 that the 1-halo term, $P_{1h}^{\text{gal}}(k) \rightarrow P_{\text{shot}}^{\text{halo}}$ for wavenumbers $k \rightarrow 0$, and $P_{1h}^{\text{gal}}(k) \rightarrow P_{\text{shot}}^{\text{gal}}$ for wavenumbers $k \rightarrow \infty$. The shape of $P_{1h}^{\text{gal}}(k)$ on intermediate scales depends on the average weight distribution of galaxies inside of the haloes. $P_{1h}^{\text{gal}}(k)$ is plotted in red in Fig. 1.

$\hat{u}_h(k)$ for a given halo is related to the underlying halo profile that the galaxies in the halo are thought to be sampled from, as well as the correlation of weight with position (see Appendix A2 for explanation). Note that $\hat{u}_h(k)$ differs from the actual distribution of SFRs in a halo, which we define as $\hat{v}_h^{(s)}(k)$ in Section 2.4.2. $U(k)^2$ is a weighted average of the individual $\hat{u}_h(k)^2$ profiles (Eq. (32)). To compute $U(k)$ from Eq. (1), we use the values for $P_{\text{shot}}^{\text{halo}}$ and $P_{\text{shot}}^{\text{gal}}$ from the previous section, and the 2-halo term is computed by subtracting the halo shot noise from the halo power spectrum, as in Section 5.1. We plot $U(k)^2$ measured in TNG at $z = 1.5$ as the red line in Fig. 19; $U(k)^2 \rightarrow 1$ for $k \rightarrow 0$ by construction.

$U(k)^2$ starts to deviate noticeably from 1 for $\log k \gtrsim -0.5$,

signalling the scale below which the galaxy power spectrum starts to deviate from the halo power spectrum (Fig. 18). We can repeat the calculation, this time restricting it to galaxies in haloes within a narrow mass range. Although haloes of mass $\log M_{\text{vir}} \sim 12 - 12.5$ (pink dotted line) dominate the CSFRD, $U(k)^2$ computed for the case including all haloes is more similar to that for haloes with a slightly higher mass, $\log M_{\text{vir}} \sim 13$. This makes sense, since such haloes have significantly more star formation in satellites than the lower-mass haloes, as we showed in Fig. 7.

As the 2-halo term for the galaxy power spectrum differs on small scales from the 2-halo term computed from the halo power spectrum, the shape of $U(k)^2$ may be less accurate in the range $-0.5 \lesssim \log k \lesssim 0.5$. For $\log k \lesssim -0.5$, $U(k)^2 = 1$, so they are equivalent. For $\log k \gtrsim 0.5$, the 2-halo term is negligible due to halo exclusion, therefore the error has little impact on the total power spectrum on these scales.

$U(k)$ is a weighted average of the SFR distribution in haloes. What does this distribution look like for a single halo? The distribution of the *dark matter density* follows the NFW profile (Navarro et al. 1997b),

$$\rho(r) = \frac{\rho_0}{r/r_s (1 + r/r_s)^2}, \quad (37)$$

where $r_s = r_{\text{vir}}/c$ is called the scale radius, c the concentration of the halo, and ρ_0 is a normalisation that sets M_{vir} . As a first approximation, we might assume that the subhaloes that host satellites follow a similar profile. If, additionally, we ignore the fact that the contribution of a satellite is weighted by its SFR, then the halo profile is simply the Fourier transform, $\hat{u}(k)$, of the NFW profile – apart from the overall normalisation. However, the distribution of subhaloes is not generally the same as that of the mass (e.g. Zavala & Frenk 2019) and satellites *are weighted* by their SFR. Nevertheless, the NFW profile might be a reasonable first guess for $\hat{u}(k)$, but the parameters r_s and c may be different from that of the mass. There is also a third parameter to consider: the radius to which we integrate when Fourier transforming the profile. This radius does not have to be the virial radius, r_{vir} , and will be denoted by r_{max} .

Equation (32) relates the halo profile of haloes, $\hat{u}(k)$, to the function $U(k)^2$. Even if the $\hat{u}(k)$'s for all haloes were well-described by an NFW profile, there is no reason that $U(k)$ would be well-described by that profile. Nevertheless, we can find fitting parameters $r_{\text{vir}} = 0.5$ cMpc h^{-1} , $c = 137$, and $r_{\text{max}} = 1.06$ cMpc h^{-1} so that (the Fourier transform of) the NFW profile roughly reproduces $U(k)$ from TNG: the fit is shown by the dashed black line in Fig. 19.

The values for r_{vir} and r_{max} are not unexpected, but the best-fitting value of $c \sim 137$ for the concentration is unexpectedly high – we would have expected a value of around 10 at most, based on typical halo mass-concentration relations (e.g. Klypin et al. 2016). Why is such a high concentration required? One factor is that the $\hat{u}(k)$ is contributed to by haloes of all masses, and therefore sizes, but we integrate the NFW profile to $r_{\text{max}} = 1.06$ cMpc h^{-1} . For many of the smaller haloes, there will be no star formation at larger radii, and this is instead accounted for by increasing the concentration. Another factor is that the central galaxy is always at the ‘centre’ of the halo. This galaxy contributes to the galaxy power spectrum, $P_{\text{tot}}^{\text{gal}}$, and hence to $U(k)$, but it may be inappropriate to include it in the NFW profile. Therefore, we next

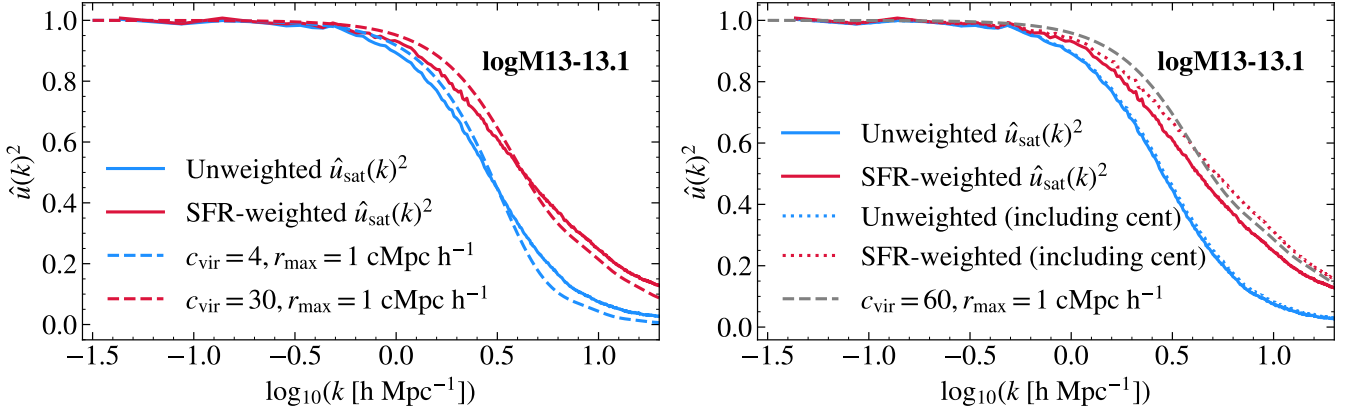


Figure 20. *Left panel:* Square of the Fourier transform of the halo profiles, $\hat{u}_{\text{sat}}(k)^2$, for satellites in haloes of mass $\log M_{\text{vir}} \in [13, 13.1]$ in TNG at $z = 1.5$. The *solid blue line* is the profile when satellites with non-zero SFR are given equal weight, and the *solid red line* for when satellites are weighted by their SFR. *Dashed lines* are NFW fits, with the legend stating the best-fit NFW parameters. The virial radius is given by $r_{\text{vir}} = 0.5 \text{ cMpc h}^{-1}$ for all the NFW fits. *Right panel:* *Solid lines* are the same as in the left panel. *Dotted lines* show (the Fourier transform squared of) the halo profiles if the central galaxy is included as well. The *dashed grey line* is an NFW fit to the *dotted red line* (the case where both the central galaxy and satellites are included and weighted by their SFR). Including the central galaxy has little effect in the unweighted case (i.e., the *dotted blue line* is nearly identical to the *blue solid line*), but the effect is greater in the weighted case (i.e., the *dotted red line* has a different shape from the *red solid line*).

consider the profile $\hat{u}_{\text{sat}}(k)$, which includes satellite galaxies only (Eq. (B4) writes the 1-halo term in terms of $\hat{u}_{\text{sat}}(k)$). See also McDonough & Brainerd (2022) for a comparison of the satellite distribution in TNG with NFW-like profiles.

We compute the power spectrum of satellite galaxies in haloes in a narrow range of masses, $\log M_{\text{vir}} \in [13, 13.1]$ (at $z = 1.5$), for both the case where the satellite galaxies are at their fiducial positions and for the case where their contribution is assigned to the centre of their respective haloes. We use these power spectra to compute $\hat{u}_{\text{sat}}(k)$ (using Eq. (1)). The $\hat{u}_{\text{sat}}(k)$ for this case is plotted as solid lines in both panels of Fig. 20: the blue line corresponds to weighting each satellite equally (provided the satellite’s SFR is non-zero), while the red line corresponds to weighting each satellite by its SFR (the latter being relevant to LIM). Dashed lines in the left panel show NFW profiles, with the legend including the best-fitting values of the NFW parameters, and $r_{\text{vir}} = 0.5 \text{ cMpc h}^{-1}$ for all the NFW fits. The case of equal weighting (blue lines) yields a reasonable concentration of $c \sim 4$ (see, e.g., Klypin et al. 2016; Child et al. 2018 for measurements of the concentration-mass relation of dark matter haloes). However, weighting satellites by their SFR (red lines) yields a much higher concentration of $c \sim 30$.

Note that we extrapolate the NFW profile beyond the halo’s virial radius (we use $r_{\text{max}} = 1 \text{ cMpc h}^{-1}$, which is much larger than the virial radius of the haloes in the mass range shown in Fig. 20). If, instead, we Fourier transform the NFW profile only up to the virial radius (0.5 cMpc h^{-1}), we find that the resulting $\hat{u}_{\text{sat}}(k)$ differs significantly from that measured from the simulation. This is because there are satellite galaxies with non-negligible SFR outside the virial radii of haloes. Although the NFW profile does not fit the distribution (of dark matter or galaxies) well outside the virial radius, integrating past the virial radius is still better than ignoring the contribution from outside the virial radius completely. Zhou & Han (2023, 2024) show that using the Einasto (1969) profile – rather than the NFW profile – and extrapolating it beyond the

halo’s virial radius, improves the fit to the non-linear matter power spectrum obtained within the halo model. Both their findings and ours suggest that the matter or galaxy distribution outside the virial radius needs to be modelled to yield accurate 1-halo terms. We further note that we used a single value of the NFW parameters for haloes of a given mass – whereas it is known that there is scatter in concentration (Bullock et al. 2001) and some haloes may not follow the NFW profile well (Jing 2000). Using the Einasto profile and accounting for scatter may improve the fits to the 1-halo term.

As mentioned previously, the best-fitting value of c is significantly higher for the case where satellites are weighted by their SFR. This suggests that the SFRs of satellites are not independent of their position in the halo. The increased concentration suggests that there is increased star formation occurring in galaxies near the centre of the halo compared to in its outskirts, relative to the dark matter. We also find that the SFRs of distinct satellite galaxies are correlated with each other, a finding we discuss in Appendix A2.

In the right panel of Fig. 20, we plot both $\hat{u}_{\text{sat}}(k)$, the halo profile of satellites only (solid lines) – i.e. after removing the central galaxy – as well as $\hat{u}(k)$ (dotted lines) which includes the contribution of the central galaxy. Including the central galaxy does not change the profile much in the unweighted case (blue dotted compared to blue solid line), but the effect is more pronounced in the SFR-weighted case (red dotted compared to red solid line in the right panel). Including the central increases the best-fitting value of the concentration from $c = 30$ to $c = 60$. Since the central galaxy is always at the centre of the halo, it might be physically more meaningful to add a delta function to the profile to represent the central galaxy – rather than increasing c . We discuss this in Appendix A2.

5.3 Model summary

We briefly summarise the total model for the galaxy power spectrum, $P_{\text{tot}}^{\text{gal}}$, that we introduced in Eq. (1) and discussed in the previous sections. All equations are repeated in Table 1.

The galaxy power spectrum is the sum of a 2-halo term, P_{2h}^{gal} , and a 1-halo term, P_{1h}^{gal} . The 2-halo term, P_{2h}^{gal} , captures the clustering of galaxies in distinct haloes. On large-scales, it captures the clustering of the dark matter haloes themselves. We describe P_{2h}^{gal} as a biased version of the non-linear matter power spectrum, with bias b , on scales larger than that of haloes. On scales comparable to or smaller than the sizes of haloes, power is suppressed due to halo exclusion. Halo exclusion is modelled by assuming that the distribution of exclusion distances has a lognormal shape, parametrised by $\log_{10}(d_0)$ – the logarithmic mean of the exclusion distance – and σ – the logarithmic scatter around the mean. These two parameters define the function f , the probability of finding two haloes at distance greater than r (see Table 1).

The 1-halo term, P_{1h}^{gal} , has three independent contributions. On scales much larger than d_0 , P_{1h}^{gal} is a constant, set by the *halo* shot noise. On scales much smaller than d_0 , P_{1h}^{gal} is a constant, set by the *galaxy* shot noise. The smooth interpolation of P_{1h}^{gal} between its asymptotes is regulated by the mean profiles of satellites in haloes, when they are weighted by their SFR. For haloes within a small range of masses, this profile can be fit with an NFW profile, provided that (i) the profile is extrapolated to r_{max} , a radius well beyond the virial radius of the halo, and (ii) the concentration c of the NFW profile is much higher than that of the matter density. The 1-halo term can also be fitted by an NFW profile if all haloes are included. The halo profile is denoted by \hat{u} in Table 1.

6 SUMMARY AND CONCLUSIONS

Line-intensity mapping (LIM) is an emerging technique for efficiently mapping the three-dimensional spatial distribution of galaxies (e.g. Kovetz et al. 2017). LIM promises to measure this distribution on the very large scales that are still in the linear regime, enabling inferences about the primordial power spectrum and the nature of the initial perturbations (e.g. primordial non-Gaussianity or features imprinted during inflation). LIM surveys may also have sufficient spatial resolution to measure the distribution of galaxies on much smaller scales, and these measurements could be used to constrain theories of galaxy formation.

In this paper, we investigate the power spectrum of galaxies when they are weighted by their star formation rate (SFR). This is relevant to LIM because the luminosity of emission lines from galaxies mapped in LIM surveys is often strongly correlated with their SFR. Our analysis is general but with a focus on redshift $z \sim 1.5$, an ideal target for LIM surveys based on the H α line. We mostly analyse the 300 Mpc realisation of the ILLUSTRISTNG simulation (Pillepich et al. 2018), hereafter TNG), but also use the higher resolution 100 Mpc realisation as well as the EAGLE simulation (Schaye et al. 2015). Our aim is to fit the simulated power spectrum – from large linear scales, to small, very non-linear scales – in terms of a set of parameters with a clear physical meaning.

Galaxies in the simulations are labelled as centrals or satellites. This distinction is relevant because the galaxy power

spectrum depends on the spatial distribution of the SFR of satellites in a halo on scales comparable to or smaller than that of haloes. We therefore write the total galaxy power spectrum as a sum of two terms: a 1-halo term – quantifying how satellites are distributed in haloes – and a 2-halo term – which quantifies how haloes are clustered. This dissection is inspired by the halo model (Cooray & Sheth 2002) for the total matter power spectrum. We show that the 1-halo term can be written in terms of a shot noise and halo density profile parameter. The 2-halo term is written in terms of bias with respect to the non-linear matter distribution and a function describing halo exclusion.

Our main findings are as follows:

(i) The galaxy power spectrum, in which galaxies are weighted by their SFR, is fitted well by a model that incorporates biased clustering of haloes compared to the non-linear matter power spectrum, halo exclusion, shot noise, and a 1-halo term that captures the spatial distribution of satellite galaxies in haloes.

(ii) Satellite galaxies contribute ~ 30 per cent to the total star formation rate density (Fig. 9) in TNG at $z \sim 1.5$. Neglecting their contribution leads to an underestimate of the galaxy power spectrum by ~ 30 per cent on large scales (Fig. 11) – even when the power spectrum is normalised by the mean SFR. On average, the effect of satellite galaxies increases with decreasing redshift (Fig. 12).

(iii) Satellites dominate the SFR in haloes with virial mass greater than $\log M_{\text{vir}} [\text{M}_{\odot} \text{h}^{-1}] \sim 12.5$ (Fig. 7). This is primarily due to two factors: the quenching of the SFR of the central galaxy due to feedback from its accreting supermassive black hole (AGN feedback), and the increase in both the number and SFRs of satellites with increasing halo mass.

(iv) We test the impact of the spatial distribution of satellites on the power spectrum by summing the SFR of all galaxies in a halo and assigning it to the position of the central galaxy. The resulting power spectrum differs by less than 1 per cent from the original power spectrum (in which haloes are resolved in central and satellite galaxies) on scales $\log_{10}(k [\text{h Mpc}^{-1}]) \lesssim -0.5$ (Fig. 14). Therefore, assigning a single luminosity to the centre of each halo is sufficient for reproducing the large-scale power spectrum, unless one wants to probe the 1-halo term.

(v) We fit the 2-halo term by taking into account halo exclusion and non-linear halo bias (Fig. 16). Approximating the distribution of exclusion distances using a lognormal distribution works well.

(vi) Shot noise – arising from finite sampling of a distribution – is scale-dependent: it is set by the SFRs of galaxies on small scales, and the SFRs of haloes on large scales (Fig. 1; see also Baldauf et al. 2013). On the largest scales in the TNG300 box ($\log_{10}(k [\text{h Mpc}^{-1}]) \sim -1.5$), the shot noise is still not negligible, therefore care should be taken when making the assumption that the shot noise is negligible on “large scales”.

(vii) We investigated the effect of weighting satellites by their SFR and including the SFR of the central galaxy – as appropriate for LIM modelling – on the halo profile. Although the halo profile can be fit by an NFW profile, that profile should be extrapolated beyond the halo’s virial radius, and the best-fit value of the concentration is much higher than that of the dark matter profile (Fig. 20).

We have made several approximations that could be im-

Model Parameters for fitting the galaxy power spectrum, $P_{\text{tot}}^{\text{gal}}(k)$			
$P_{\text{tot}}^{\text{gal}}(k) = P_{2h}(k, \hat{v}_h^{(s)}(\mathbf{k})) + U(k)^2(P_{\text{shot}}^{\text{halo}} - P_{\text{shot}}^{\text{gal}}) + P_{\text{shot}}^{\text{gal}}$ (Eq. (1))			
2- and 1-halo terms	Component	Parameter	Value at $z \sim 1.5$
2-halo term, $P_{2h}^{\text{gal}}(k)$ $= 4\pi \int_0^\infty f(r) \xi'(r) \frac{\sin(kr)}{kr} r^2 dr$ (Eq. (20))	Halo exclusion $f(r) = 1 - \frac{1}{2} \left(1 + \text{erf} \left[\frac{\log_{10}(r/d_0)}{\sqrt{2}\sigma} \right] \right)$ (Eq. (36))	r_0	0.74 cMpc h ⁻¹
	Non-linear bias $\xi'(r) = b^2 \xi_m(r)$	σ	0.17 dex
		b	2.0
1-halo term, $P_{1h}^{\text{gal}}(k)$ $= U(k)^2(P_{\text{shot}}^{\text{halo}} - P_{\text{shot}}^{\text{gal}}) + P_{\text{shot}}^{\text{gal}}$ (Eq. (31))	Halo shot noise	$P_{\text{shot}}^{\text{halo}}$	300 (h Mpc ⁻¹) ³
	Galaxy shot noise	$P_{\text{shot}}^{\text{gal}}$	150 (h Mpc ⁻¹) ³
	Halo profile: $U(k) = \hat{u}_{\text{NFW}}(k) \propto \int_0^{r_{\text{max}}} \frac{1}{(r/r_s)(1+r/r_s)^2} \exp(-ik \cdot r) d^3r$	r_{max} r_s	1.05 cMpc h ⁻¹ 0.0036 cMpc h ⁻¹ ($c = 137$ for $r_{\text{vir}} = 0.5$ cMpc h ⁻¹)

Table 1. Parametrisation of the galaxy power spectrum, $P_{\text{tot}}^{\text{gal}}(k)$, in terms of a 2-halo and 1-halo term. The 2-halo term is parametrised in terms of the bias, b , with respect to the non-linear matter correlation function, ξ_m (which we compute using HALOFIT, Takahashi et al. 2012) and the function $f(r)$ that captures halo exclusion. The latter is parametrised by the mean exclusion distance, d_0 , and the standard deviation σ around the lognormal distribution of exclusion distances. The 1-halo term depends on the halo and galaxy shot noise terms, and the function u that describes how star-forming satellites are distributed in haloes, on average. u can be fitted with an NFW profile. The values for all parameters in the last column are for the TNG simulation at redshift $z = 1.5$.

proved upon. We have only considered a linear relation between SFR and line luminosity, yet the luminosity of emission lines can also depend on other properties, such as metallicity. For example, satellites can have higher metallicity than central galaxies (Bahé et al. 2017), which can affect luminosities of emission lines such as [OIII], in which case satellites should be considered even more carefully. Although AGN feedback may quench the SFR of central galaxies, they themselves can also contribute to line luminosities – an effect we have not considered here. We have also not considered the signals in redshift space. The motions of satellite galaxies in large haloes causes the so-called Fingers-of-God effect (Jackson 1972) on small scales.

While we have focused on how the power spectrum is affected by satellite galaxies, it can also be affected by the dependence of the SFR on properties beyond mass – halo concentration, formation time, environment – so-called ‘assembly bias’ terms. These aspects are, to some extent, captured in the simulation, and are therefore implicitly accounted for in our fit to the simulation data. Since our model does not depend on halo mass, it is not affected by secondary halo bias. However, models which rely on a luminosity-halo mass relation will need to account for this bias.

On the largest scales probed by TNG300 (linear extent of 205 cMpc h⁻¹), sample variance limits our ability to confirm the existence of a constant bias, and for $\log_{10}(k [\text{h Mpc}^{-1}]) \gtrsim -1$, the non-linear clustering of haloes becomes significant. The haloes still trace the non-linear matter power spectrum well up to $\log_{10}(k [\text{h Mpc}^{-1}]) \lesssim 0.5$, but beyond that halo exclusion and the 1-halo term need to be taken into account to model the power spectrum. It is useful to use simulations, which naturally include these effects, to inform analytical or semi-analytical models, which are faster and more flexible

in exploring parameters. Our parametrisation for the galaxy power spectrum can also be applied to other simulations, although the best-fitting parameters may well depend on numerical resolution and the choice of subgrid galaxy formation recipes. Similarly, the same underlying model can be applied to other redshifts, in which case, a model for the scale-dependence of the halo bias relative to the matter power spectrum needs to be used.

Going to larger scales will allow cosmology to be constrained further. Therefore, the lack of linear scales probed also becomes a further motivator for surveying larger volumes, which could become more feasible with LIM. Simultaneously, while we anticipate the planning of larger scale surveys, we should maximise the value of the data from smaller scale surveys, which are more feasible in the near-term. The non-linear regime already provides us with information about structure formation, and can provide tests for cosmological models. In COMAP season 2 results (Chung et al. 2024), for instance, the shot noise and bias of the CO power spectrum have been constrained by fitting the obtained upper limit of the power spectrum on scales $-1 \lesssim \log_{10}(k [\text{h Mpc}^{-1}]) \lesssim 0$. In such analyses, one can take into account the non-linear effects discussed in this study to better extract physical information from the data.

This work provides a flexible and physically-motivated framework for modelling the galaxy power spectrum, effectively capturing nonlinearities and enabling analysis of power spectrum data from upcoming surveys.

ACKNOWLEDGEMENTS

RLJ has been supported by The University of Tokyo Fellowship. KM acknowledges JSPS KAKENHI Grant Number 23K03446, 23K20035, and 24H00004. SB is supported by the UK Research and Innovation (UKRI) Future Leaders Fellowship (grant number MR/V023381/1). This work used the DiRAC@Durham facility managed by the Institute for Computational Cosmology on behalf of the STFC DiRAC HPC Facility (www.dirac.ac.uk). The equipment was funded by BEIS capital funding via STFC capital grants ST/K00042X/1, ST/P002293/1, ST/R002371/1 and ST/S002502/1, Durham University and STFC operations grant ST/R000832/1. DiRAC is part of the National e-Infrastructure.

DATA AVAILABILITY

The IllustrisTNG data are publicly available at <https://www.tng-project.org/>. The EAGLE data are publicly available at <https://icc.dur.ac.uk/Eagle/>. We will share the scripts used in this paper upon reasonable request.

REFERENCES

- Ade P. A. R., et al., 2016, *Astronomy & Astrophysics*, 594, A13
- Artale M. C., et al., 2017, *MNRAS*, 470, 1771
- Bahé Y. M., Schaye J., Crain R. A., McCarthy I. G., Bower R. G., Theuns T., McGee S. L., Trayford J. W., 2017, *MNRAS*, 464, 508
- Baldauf T., Seljak U., Smith R. E., Hamaus N., Desjacques V., 2013, *Physical Review D*, 88
- Ballardini M., et al., 2024, *A&A*, 683, A220
- Berlind A. A., Weinberg D. H., 2002, *ApJ*, 575, 587
- Bernal J. L., Kovetz E. D., 2022, *A&ARv*, 30, 5
- Brainerd T. G., Blandford R. D., Smail I., 1996, *ApJ*, 466, 623
- Bryan G. L., Norman M. L., 1998, *ApJ*, 495, 80
- Bullock J. S., Kolatt T. S., Sigad Y., Somerville R. S., Kravtsov A. V., Klypin A. A., Primack J. R., Dekel A., 2001, *MNRAS*, 321, 559
- Cabass G., Ivanov M. M., Philcox O. H. E., Simonović M., Zaldarriaga M., 2023, *Physics Letters B*, 841, 137912
- Casas-Miranda R., Mo H. J., Sheth R. K., Boerner G., 2002, *MNRAS*, 333, 730
- Chabrier G., 2003, *PASP*, 115, 763
- Child H. L., Habib S., Heitmann K., Frontiere N., Finkel H., Pope A., Morozov V., 2018, *ApJ*, 859, 55
- Chung D. T., et al., 2024, *arXiv e-prints*, p. [arXiv:2406.07512](https://arxiv.org/abs/2406.07512)
- Clampitt J., et al., 2017, *MNRAS*, 465, 4204
- Cooray A., Sheth R., 2002, *Phys. Rep.*, 372, 1
- Crain R. A., et al., 2015, *MNRAS*, 450, 1937
- DESI Collaboration et al., 2016, *arXiv e-prints*, p. [arXiv:1611.00036](https://arxiv.org/abs/1611.00036)
- Davis M., Efstathiou G., Frenk C. S., White S. D. M., 1985, *ApJ*, 292, 371
- Doré O., et al., 2018, *arXiv e-prints*, p. [arXiv:1805.05489](https://arxiv.org/abs/1805.05489)
- Dubois Y., et al., 2014, *MNRAS*, 444, 1453
- Einasto J., 1969, *Astrophysics*, 5, 67
- Eisenstein D. J., Hu W., 1998, *The Astrophysical Journal*, 496, 605–614
- Fonseca J., Silva M. B., Santos M. G., Cooray A., 2016, *Monthly Notices of the Royal Astronomical Society*, 464, 1948
- García R., Rozo E., 2019, *MNRAS*, 489, 4170
- Garn T., et al., 2010, *MNRAS*, 402, 2017
- Gebhardt K., et al., 2021, *ApJ*, 923, 217
- Gong Y., Cooray A., Silva M. B., Zemcov M., Feng C., Santos M. G., Dore O., Chen X., 2017, *ApJ*, 835, 273
- Gong Y., Chen X., Cooray A., 2020, *ApJ*, 894, 152
- Guth A. H., 1981, *Phys. Rev. D*, 23, 347
- Guth A. H., Pi S. Y., 1982, *Phys. Rev. Lett.*, 49, 1110
- Hand N., Seljak U., Beutler F., Vlah Z., 2017, *J. Cosmology Astropart. Phys.*, 2017, 009
- Hand N., Feng Y., Beutler F., Li Y., Modi C., Seljak U., Slepian Z., 2019, nbodykit: Massively parallel, large-scale structure toolkit, Astrophysics Source Code Library, record ascl:1904.027 (ascl:1904.027)
- Hirschmann M., et al., 2023, *MNRAS*, 526, 3610
- Hockney R. W., Eastwood J. W., 1981, *Computer Simulation Using Particles*. McGraw-Hill International Book Company
- Jackson J. C., 1972, *MNRAS*, 156, 1P
- Jing Y. P., 2000, *ApJ*, 535, 30
- Jing Y. P., 2005, *The Astrophysical Journal*, 620, 559
- Jose C., Lacey C. G., Baugh C. M., 2016, *MNRAS*, 463, 270
- Kaiser N., Peacock J. A., 1991, *ApJ*, 379, 482
- Karkare K. S., et al., 2022, *Journal of Low Temperature Physics*, 209, 758
- Keating G. K., Marrone D. P., Bower G. C., Leitch E., Carlstrom J. E., DeBoer D. R., 2016, *ApJ*, 830, 34
- Keating G. K., Marrone D. P., Bower G. C., Keenan R. P., 2020, *ApJ*, 901, 141
- Kennicutt Robert C. J., 1998, *ARA&A*, 36, 189
- Klypin A., Yepes G., Gottlöber S., Prada F., Heß S., 2016, *MNRAS*, 457, 4340
- Kovetz E. D., et al., 2017, *arXiv e-prints*, p. [arXiv:1709.09066](https://arxiv.org/abs/1709.09066)
- Liddle A. R., Lyth D. H., 2000, *Cosmological Inflation and Large-Scale Structure*. Cambridge University Press
- Linde A. D., 1982, *Physics Letters B*, 108, 389
- Madau P., Dickinson M., 2014, *Annual Review of Astronomy and Astrophysics*, 52, 415–486
- Marinacci F., et al., 2018, *Monthly Notices of the Royal Astronomical Society*
- McAlpine S., et al., 2016, *Astronomy and Computing*, 15, 72
- McDonough B., Brainerd T. G., 2022, *ApJ*, 933, 161
- Mead A. J., Verde L., 2021, *MNRAS*, 503, 3095
- Mo H. J., White S. D. M., 1996, *MNRAS*, 282, 347
- Monaco P., Theuns T., Taffoni G., 2002, *MNRAS*, 331, 587
- Moradinezhad Dizgah A., Nikakhtar F., Keating G. K., Castorina E., 2022, *J. Cosmology Astropart. Phys.*, 2022, 026
- Nagaraj G., Ciardullo R., Bowman W. P., Lawson A., Gronwall C., 2023, *The Astrophysical Journal*, 943, 5
- Naiman J. P., et al., 2018, *Monthly Notices of the Royal Astronomical Society*, 477, 1206
- Navarro J. F., Frenk C. S., White S. D. M., 1997a, *ApJ*, 490, 493
- Navarro J. F., Frenk C. S., White S. D. M., 1997b, *ApJ*, 490, 493
- Nelson D., et al., 2017, *Monthly Notices of the Royal Astronomical Society*, 475, 624
- Nelson D., et al., 2019, *Computational Astrophysics and Cosmology*, 6, 2
- Padmanabhan H., Refregier A., Amara A., 2017, *MNRAS*, 469, 2323
- Pakmor R., et al., 2023, *MNRAS*, 524, 2539
- Peebles P. J. E., 1980, *The large-scale structure of the universe*. Princeton Univ. Press, Princeton, NJ
- Pénin A., Umeh O., Santos M. G., 2018, *MNRAS*, 473, 4297
- Pillepich A., et al., 2018, *MNRAS*, 473, 4077
- Piotrowska J. M., Bluck A. F. L., Maiolino R., Peng Y., 2022, *MNRAS*, 512, 1052
- Planck Collaboration et al., 2020, *A&A*, 641, A6
- Salpeter E. E., 1955, *ApJ*, 121, 161
- Schaan E., White M., 2021, *Journal of Cosmology and Astroparticle Physics*, 2021, 068

- Schaye J., et al., 2015, *MNRAS*, 446, 521
- Schaye J., et al., 2023, *MNRAS*, 526, 4978
- Schottky W., 1918, *Annalen der Physik*, 362, 541
- Schottky W., 2018, *Journal of Micro/Nanolithography, MEMS, and MOEMS*, 17, 41001
- Sefusatti E., Crocce M., Scoccimarro R., Couchman H. M. P., 2016, *Monthly Notices of the Royal Astronomical Society*, 460, 3624
- Sheth R. K., Tormen G., 1999, *MNRAS*, 308, 119
- Silva B. M., Zaroubi S., Kooistra R., Cooray A., 2017, *Monthly Notices of the Royal Astronomical Society*, 475, 1587
- Smith R. E., Scoccimarro R., Sheth R. K., 2007, *Physical Review D*, 75
- Sobral D., Best P. N., Matsuda Y., Smail I., Geach J. E., Cirasuolo M., 2012, *MNRAS*, 420, 1926
- Sobral D., Smail I., Best P. N., Geach J. E., Matsuda Y., Stott J. P., Cirasuolo M., Kurk J., 2013, *MNRAS*, 428, 1128
- Springel V., 2010, *Monthly Notices of the Royal Astronomical Society*, 401, 791–851
- Springel V., White S. D. M., Tormen G., Kauffmann G., 2001, *Monthly Notices of the Royal Astronomical Society*, 328, 726–750
- Springel V., et al., 2005a, *Nature*, 435, 629
- Springel V., et al., 2005b, *Nature*, 435, 629
- Springel V., et al., 2017, *Monthly Notices of the Royal Astronomical Society*, 475, 676
- Sun G., Hensley B. S., Chang T.-C., Doré O., Serra P., 2019, *ApJ*, 887, 142
- Symons T., Zemcov M., Bock J., Cheng Y.-T., Crill B., Hirata C., Venuto S., 2021, *The Astrophysical Journal Supplement Series*, 252, 24
- Takahashi R., Sato M., Nishimichi T., Taruya A., Oguri M., 2012, *The Astrophysical Journal*, 761, 152
- Tinker J. L., Robertson B. E., Kravtsov A. V., Klypin A., Warren M. S., Yepes G., Gottlöber S., 2010, *ApJ*, 724, 878
- Umeh O., 2017, *J. Cosmology Astropart. Phys.*, 2017, 005
- Umeh O., Maartens R., Santos M., 2016, *J. Cosmology Astropart. Phys.*, 2016, 061
- Vieira J., et al., 2020, *arXiv e-prints*, p. arXiv:2009.14340
- Villaescusa-Navarro F., et al., 2018, *ApJ*, 866, 135
- Vogelsberger M., et al., 2014, *MNRAS*, 444, 1518
- Vogelsberger M., Marinacci F., Torrey P., Puchwein E., 2020, *Nature Reviews Physics*, 2, 42
- Weinberger R., et al., 2017, *MNRAS*, 465, 3291
- Wolz L., Murray S. G., Blake C., Wyithe J. S., 2019, *MNRAS*, 484, 1007
- Wyithe J. S. B., Brown M. J. I., 2010, *MNRAS*, 404, 876
- Yuan S., et al., 2024, *MNRAS*, 530, 947
- Zavala J., Frenk C. S., 2019, *Galaxies*, 7, 81
- Zhang Y., Pullen A. R., Somerville R. S., Breyse P. C., Forbes J. C., Yang S., Li Y., Maniyar A. S., 2023, *ApJ*, 950, 159
- Zhou Y., Han J., 2023, *MNRAS*, 525, 2489
- Zhou Y., Han J., 2024, *arXiv e-prints*, p. arXiv:2407.08381
- van den Bosch F. C., More S., Cacciato M., Mo H., Yang X., 2013, *MNRAS*, 430, 725

APPENDIX A: CONTRIBUTION FROM HALO PROFILE**A1 Derivation of the 1-halo term**

Equation (29) is the 1-halo term in terms of the measured halo profile, $\hat{v}_h^{(s)}(k)$, i.e. the Fourier transform of the actual (discrete) galaxy distribution. It is common to assume that galaxies are sampled from an underlying smooth density distribution, such as the halo matter distribution with Fourier transform $\hat{u}(k)$. The functions $\hat{v}_h^{(s)}(k)$ and $\hat{u}(k)$ differ by the galaxy shot noise. To see how this comes about, we separate the 1-halo term into self-pairs and distinct pairs, where the self-pairs term gives rise to the shot noise:

$$\begin{aligned}
P_{1h,w}(k) &= \frac{1}{V} \left\langle \sum_h \sum_{g \in h} \sum_{g' \in h} W_g W_{g'} \exp[-i\mathbf{k} \cdot (\mathbf{r}_g - \mathbf{r}_{g'})] \right\rangle \\
&= \frac{1}{V} \left\langle \sum_h \sum_{g \in h} \left(\sum_{\substack{g' \in h \\ g' \neq g}} + \sum_{g'=g} \right) W_g W_{g'} \exp[-i\mathbf{k} \cdot (\mathbf{r}_g - \mathbf{r}_{g'})] \right\rangle \\
&= \frac{1}{V} \left\langle \sum_h \sum_{g \in h} \sum_{\substack{g' \in h \\ g' \neq g}} W_g W_{g'} \exp[-i\mathbf{k} \cdot (\mathbf{r}_g - \mathbf{r}_{g'})] \right\rangle + \frac{1}{V} \left\langle \sum_h \sum_{g \in h} W_g^2 \right\rangle, \tag{A1}
\end{aligned}$$

where the outer sum with index h is over haloes, and the product of sums with indices g and g' are over galaxies in halo h . The second term in the last line arises from the case where $g = g'$ and is the shot noise term. To describe the $g \neq g'$ term, we define

$$|\hat{u}(k)|^2 = \frac{\left\langle \sum_{g \in h} \sum_{g' \neq g \in h} W_g W_{g'} \exp[-i\mathbf{k} \cdot (\mathbf{r}_g - \mathbf{r}_{g'})] \right\rangle}{\sum_{g \in h} \sum_{g' \neq g \in h} W_g W_{g'}}. \tag{A2}$$

We explain in Appendix A2 how this term relates to the halo profile. This allows us to rewrite the first term of Eq. (A1) as

$$\begin{aligned}
&\frac{1}{V} \sum_h \sum_{g \in h} \sum_{\substack{g' \in h \\ g' \neq g}} W_g W_{g'} |\hat{u}(k)|^2 \\
&= \frac{1}{V} \sum_h \sum_{g \in h} \left(\sum_{g' \in h} - \sum_{\substack{g' \in h \\ g'=g}} \right) W_g W_{g'} |\hat{u}(k)|^2 \\
&= \frac{1}{V} \sum_h \left(\sum_{g \in h} W_g \sum_{g' \in h} W_{g'} - \sum_{g \in h} W_g^2 \right) |\hat{u}(k)|^2 \\
&= \frac{1}{V} \sum_h \left(W_h^2 - \sum_{g \in h} W_g^2 \right) |\hat{u}(k)|^2. \tag{A3}
\end{aligned}$$

This result motivates us to define

$$U(k)^2 \equiv \frac{\sum_h (W_h^2 - \sum_{g \in h} W_g^2) |\hat{u}(k)|^2}{\sum_h (W_h^2 - \sum_{g \in h} W_g^2)}. \tag{A4}$$

Substituting this into Eq. (A3) gives

$$\begin{aligned}
&\frac{1}{V} \sum_h \left(W_h^2 - \sum_{g \in h} W_g^2 \right) U(k)^2 \\
&= \frac{1}{V} \left(\sum_h W_h^2 - \sum_{g \in G} W_g^2 \right) U(k)^2 \\
&= (P_{\text{shot},I}^{\text{halo}} - P_{\text{shot},I}^{\text{gal}}) U(k)^2, \tag{A5}
\end{aligned}$$

where

$$P_{\text{shot},I}^{\text{halo}} = \frac{1}{V} \sum_h W_h^2 \tag{A6}$$

is the *halo* shot noise. Equation (A5) gives the first term in Eq. (31).

A2 Relating the spatial dependence of the 1-halo term to the halo profile

We stated in Appendix A1 that the function $\hat{u}(k)$ given by Eq. (A2) can be related to the halo profile. Here, we investigate in what way they are related.

First, we assume that satellites in the same halo are uncorrelated with each other. This simplifies Eq. (A2) to

$$|\hat{u}(k)|^2 = \frac{\sum_{g \in h} \sum_{g' \neq g \in h} \langle W_g \exp[-i\mathbf{k} \cdot \mathbf{r}_g] \rangle \langle W_{g'} \exp[-i\mathbf{k} \cdot \mathbf{r}_{g'}] \rangle}{\sum_{g \in h} \sum_{g' \neq g \in h} W_g W_{g'}}. \quad (\text{A7})$$

Next, we assume that the weight and position of a satellite are uncorrelated, yielding

$$\begin{aligned} |\hat{u}(k)|^2 &= \frac{\sum_{g \in h} \sum_{g' \neq g \in h} \langle W_g \rangle \langle \exp[-i\mathbf{k} \cdot \mathbf{r}_g] \rangle \langle W_{g'} \rangle \langle \exp[-i\mathbf{k} \cdot \mathbf{r}_{g'}] \rangle}{\sum_{g \in h} \sum_{g' \neq g \in h} W_g W_{g'}} \\ &= \frac{\sum_{g \in h} \sum_{g' \neq g \in h} \langle \exp[-i\mathbf{k} \cdot \mathbf{r}_g] \rangle \langle \exp[-i\mathbf{k} \cdot \mathbf{r}_{g'}] \rangle}{N_g(N_g - 1)}, \end{aligned} \quad (\text{A8})$$

where N_g is the number of galaxies in halo h . Not surprisingly, $\hat{u}(k)$ no longer depends on the weights. Under these assumptions, $\hat{u}(k)$ should be the Fourier transform of the mean satellite distribution.

We find that weighting the galaxies by their SFR changes the shape of $\hat{u}(k)$ in TNG: the weight and position *are* correlated in TNG. In that case, we can rewrite Eq. (A7) by partitioning the sum into bins split by position as follows:

$$|\hat{u}(k)|^2 = \frac{\sum_{R_p} \sum_{g \in R_p} \langle W_{R_p} \rangle \langle \exp[-i\mathbf{k} \cdot \mathbf{r}_g] \rangle \sum_{R_q} \sum_{g' \neq g \in R_q} \langle W_{R_q} \rangle \langle \exp[-i\mathbf{k} \cdot \mathbf{r}_{g'}] \rangle}{\sum_g \sum_{g' \neq g} W_g W_{g'}}, \quad (\text{A9})$$

where R_p denotes the radial bin $R_p = [r_p, r_p + dr]$. We have assumed that within each bin, the weights are sampled independently. In this case, the weighted $\hat{u}(k)$ can be considered to be the same as multiplying the number density profile by the mean weight distribution.

Our motivation for rewriting $\hat{u}(k)$ is that we want to separate how satellites are distributed spatially from how their weights are distributed. For example, the spatial distribution might follow an NFW profile, but their weights are position dependent – so that $\hat{u}(k)$ is *not* (the Fourier transform of) an NFW profile.

We want to test whether multiplying an NFW profile by the mean weight distribution as a function of radius can properly predict the weighted $\hat{u}(k)$. In the tests in this Appendix, we consider TNG but with galaxies outside the virial radii of the haloes removed, so that there is no additional complication due to the FOE halo is being slightly different from the spherical overdensity halo.

The $\hat{u}(k)^2$ corresponding to this weighted NFW profile is shown by the dashed grey line in Fig. A1. We use the same NFW parameters as that corresponding to the dashed blue line in the left panel of Fig. 20 ($c = 4$, $r_{\text{vir}} = 0.5 \text{ cMpc h}^{-1}$, $r_{\text{max}} = 1 \text{ cMpc h}^{-1}$). This NFW profile describes the number density profile, while the weight distribution takes into account the correlation of the SFRs with distance from the centre of the halo. The weighted $\hat{u}(k)$ measured in TNG is shown by the red line, indicating that it still deviates from the prediction (dashed grey line). However, we find that by shuffling the satellites between haloes, we can reproduce the prediction. The shuffled case is shown by the brown line in the left panel of Fig. A1, which is close to the dashed grey line, which represents the prediction given by the NFW profile multiplied by the mean weight distribution. The fact that the original TNG $\hat{u}(k)$ (the solid red line in the left panel of Fig. A1) deviates from the prediction suggests that the SFRs of satellites within the same halo are correlated with each other, therefore the assumption of independent sampling is not quite valid. Closer examination shows that the difference between the unshuffled and shuffled cases is mostly caused by a few haloes with highly star-forming satellites close to the centre.

In the right panel of Fig. A1, we investigate the effect of the central galaxy: the red solid line is TNG without central galaxies, while the dotted line is TNG with the central galaxy included. The difference between the two red lines is not very large, implying that the central galaxy has little impact on the profile, at least for this halo mass. The dashed grey line is repeated from the left panel and is an NFW profile with $c = 4$, multiplied by the average weight of galaxies as function of radius – the function $w(r)$. This profile deviates a lot from the measured profile. We try to account for central star formation – either from a central, or from highly star-forming satellites near the centre – by adding a Gaussian profile to the SFR-weighted model: this yields the black dashed line. This improved model reproduces TNG quite well. Table A1 summarises the model parameters.

In Section 5.2.2, we found that the unweighted power spectrum resembles the Fourier transform of an NFW profile with concentration typical of the dark matter profile for haloes of that mass, but applying weighting changes $\hat{u}(k)$. To fit the weighted $\hat{u}(k)$, we used an NFW profile with high concentration, which seems somewhat unphysical. In this Appendix, we have provided an alternative fit which can be decomposed into the contribution from the number density distribution, the correlation of weight with distance from centre, and the contribution from the central galaxies. Using this fit may allow a more physical interpretation of how the star formation is distributed in haloes.

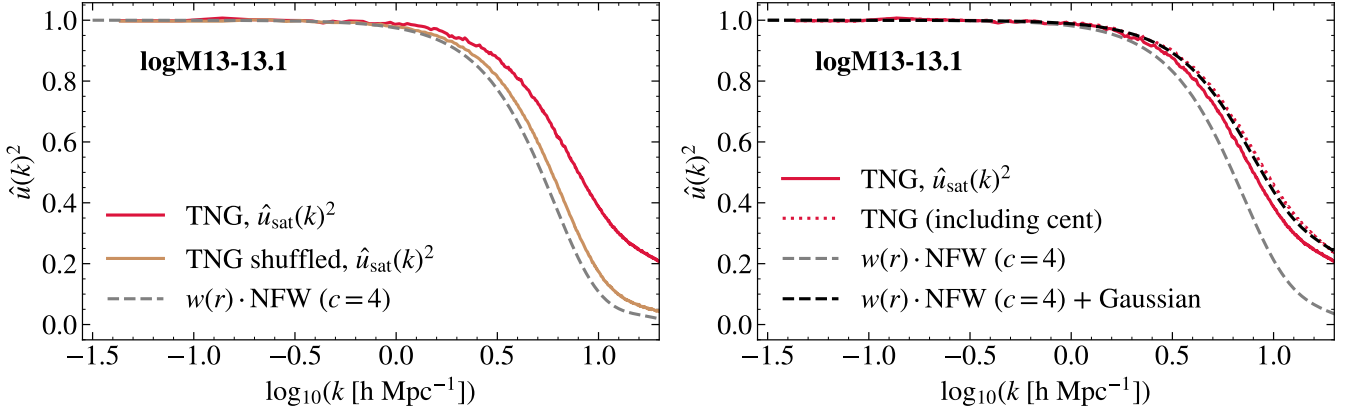


Figure A1. *Left panel:* The *solid red line* is the weighted halo profile, $\hat{u}(k)^2$, computed using the satellite galaxies in haloes with virial mass in a narrow range around $\sim 10^{13} M_{\odot}$ in the TNG simulation. The *brown line* is also from the simulation, but we have randomly reassigned satellites to these same haloes. The *grey line* is the model, in which satellites are distributed according to an NFW profile with concentration $c = 4$, and assigned the position-dependent average weight as measured in TNG. The *red and brown lines* differ substantially, signalling that there are correlations between the SFRs of satellites in the same halo. The model describes the shuffled case very well. *Right panel:* The *solid red and dashed grey lines* are the same as in the left panel. The *dotted red line* shows the $\hat{u}(k)^2$ for the original TNG simulation where the central galaxy has been included. This is fitted well when adding a Gaussian function to the centre of the halo in addition to the weighted NFW profile represented by the *dashed grey line*.

Model Parameters of 1-halo term			
Model component	Equation of component	Parameter	Value at $z \sim 1.5$
Number density profile	NFW $u_{\text{NFW}}(r) \propto \frac{1}{(r/r_s)(1+r/r_s)^2}$	r_s	0.125 cMpc h ⁻¹ ($c = 4$ for $r_{\text{vir}} = 0.5$ cMpc h ⁻¹)
Weight profile	$w(r) = a \exp(-br) + c$	a b c	1.18 1.01 h cMpc ⁻¹ -5.88
Central profile	Gaussian $G(r) = \frac{1}{\sqrt{2\pi}\sigma} \exp\left[-\frac{1}{2}\left(\frac{r-\mu}{\sigma}\right)^2\right]$	σ $\mu = 0$	0.001 cMpc h ⁻¹
Total profile	$u(r) = A \cdot w(r) \cdot u_{\text{NFW}}(r) + B \cdot G(r)$ $\hat{u}(k) = \int_0^{r_{\text{max}}} u(r) \exp(-ik \cdot r) d^3r$	A B r_{max}	1/3 2/3 0.5 cMpc h ⁻¹

Table A1. Halo profile, $\hat{u}(k)$, broken down into the contribution from the number density distribution of satellites, given by $u_{\text{NFW}}(r)$, the average weight distribution as a function of radius, $w(r)$, and the contribution from the central galaxy or satellites near the centre, modelled using a Gaussian function, $G(r)$. While the simulated $\hat{u}(k)$ may be approximated using a single NFW profile (but with very high concentration), the fit for $\hat{u}(k)$ presented in this table allows for a more physical interpretation of the distribution of SFR in the halo.

APPENDIX B: SEPARATING CENTRALS FROM SATELLITES

The weights distribution separated into the contribution from central and satellite galaxies is given by

$$w(\mathbf{r}) = \sum_{h=1}^{N_h} \left[W_{h,c} \delta^{(D)}(\mathbf{r} - \mathbf{r}_{h,c}) + \sum_{s=1}^{N_{\text{sat},h}} W_{h,s} \delta^{(D)}(\mathbf{r} - \mathbf{r}_{h,s}) \right], \quad (\text{B1})$$

where the outer summation is over all N_h halos in the volume V , the inner summation is over the $N_{\text{sat},h}$ satellites of halo h . The power spectrum, $P_{\text{tot}} = V \langle \hat{w}(\mathbf{k}) \hat{w}(-\mathbf{k}) \rangle$, can be separated into the case where these halos are the same, $h = h'$, and the case where they are different, $h \neq h'$, yielding the 1-halo term, P_{1h} , and 2-halo term, P_{2h} , respectively. The 1-halo term consists of a shot noise term due to centrals only, a central-satellite term, and a satellite-satellite term,

$$\begin{aligned} P_{1h,w}(k) = & \frac{1}{V} \underbrace{\sum_h W_{h,c}^2}_{\text{central}} + \frac{1}{V} \underbrace{\left\langle \sum_h W_{h,c} \sum_s W_{h,s} \left(\exp[-i\mathbf{k} \cdot (\mathbf{r}_{h,s} - \mathbf{r}_{h,c})] + \exp[i\mathbf{k} \cdot (\mathbf{r}_{h,s} - \mathbf{r}_{h,c})] \right) \right\rangle}_{\text{central-satellite (same halo)}} \\ & + \frac{1}{V} \underbrace{\left(\sum_h \sum_s W_{h,s}^2 + \left\langle \sum_h \sum_{\substack{s,s' \\ s \neq s'}} W_{h,s} W_{h,s'} \exp[-i\mathbf{k} \cdot (\mathbf{r}_{h,s} - \mathbf{r}_{h,s'})] \right\rangle \right)}_{\text{satellite-satellite (same halo)}}. \end{aligned} \quad (\text{B2})$$

Let

$$\hat{u}_{\text{sat},h}(k) = \frac{\sum_s \langle W_{h,s} \exp[-i\mathbf{k} \cdot (\mathbf{r}_{h,s} - \mathbf{r}_{h,c})] \rangle}{\sum_s W_{h,s}}. \quad (\text{B3})$$

Assuming the positions and weights of satellites are uncorrelated, such that $\langle W_s W_{s'} \exp[-i\mathbf{k} \cdot (\mathbf{r}_s - \mathbf{r}_{s'})] \rangle = \langle W_s \exp[-i\mathbf{k} \cdot (\mathbf{r}_s - \mathbf{r}_c)] \rangle \langle W_{s'} \exp[i\mathbf{k} \cdot (\mathbf{r}_{s'} - \mathbf{r}_c)] \rangle$ when $s \neq s'$, we can substitute $\hat{u}_{\text{sat},h}(k)$ into Eq. (B2), giving

$$\begin{aligned} P_{1h,w}(k) = & \frac{1}{V} \underbrace{\left\{ \sum_h \left(W_{h,c}^2 + \sum_s W_{h,s}^2 \right) \right\}}_{P_{\text{shot},w}^{\text{gal}}} + \frac{1}{V} \left\{ \sum_h W_{h,c} \sum_s W_{h,s} (\hat{u}_{\text{sat}}(k) + \hat{u}_{\text{sat}}(-k)) \right\} \\ & + \frac{1}{V} \left\{ \sum_h \sum_{\substack{s,s' \\ s \neq s'}} W_{h,s} W_{h,s'} \hat{u}_{\text{sat}}(k) \hat{u}_{\text{sat}}(-k) \right\}. \end{aligned} \quad (\text{B4})$$

In the limit where $k \rightarrow \infty$, such that $\hat{u}_{\text{sat}}(k) \rightarrow 0$, this tends to $P_{\text{shot},w}^{\text{gal}}$. In the limit where $k \rightarrow 0$, such that $\hat{u}_{\text{sat}}(k) \rightarrow 1$, we have

$$\begin{aligned} P_{1h,w}(k \rightarrow 0) = & \frac{1}{V} \sum_h \left(W_{h,c}^2 + \sum_s W_{h,s}^2 + 2W_{h,c} \sum_s W_{h,s} + \sum_{\substack{s,s' \\ s \neq s'}} W_{h,s} W_{h,s'} \right) \\ = & \frac{1}{V} \sum_h \left(W_{h,c} + \sum_s W_{h,s} \right)^2 \\ = & P_{\text{shot},w}^{\text{halo}}. \end{aligned} \quad (\text{B5})$$

The 2-halo term similarly consists of a term due to the clustering of centrals, the clustering of centrals with satellites in

another halo, and the clustering of satellites in one halo with satellites in another halo.

$$\begin{aligned}
P_{2h,w}(k) &= \frac{1}{V} \left\langle \underbrace{\sum_{\substack{h,h' \\ h \neq h'}} W_{h,c} W_{h',c} \exp[-i\mathbf{k} \cdot (\mathbf{r}_{h,c} - \mathbf{r}_{h',c})]}_{\text{central-central (different haloes)}} \right\rangle \\
&+ \frac{1}{V} \left\langle \underbrace{\sum_{\substack{h,h' \\ h \neq h'}} W_{h,c} \exp[-i\mathbf{k} \cdot (\mathbf{r}_{h,c} - \mathbf{r}_{h',c})] \sum_{s' \in h'} W_{h',s'} \exp[i\mathbf{k} \cdot (\mathbf{r}_{h',s'} - \mathbf{r}_{h',c})] + cc}_{\text{central-satellite (different haloes)}} \right\rangle \\
&+ \frac{1}{V} \left\langle \underbrace{\sum_{\substack{h,h' \\ h \neq h'}} \exp[i\mathbf{k} \cdot (\mathbf{r}_{h',c} - \mathbf{r}_{h,c})] \sum_{s \in h} W_{h,s} \exp[-i\mathbf{k} \cdot (\mathbf{r}_{h,s} - \mathbf{r}_{h,c})] \sum_{s' \in h'} W_{h',s'} \exp[i\mathbf{k} \cdot (\mathbf{r}_{h',s'} - \mathbf{r}_{h',c})]}_{\text{satellite-satellite (different haloes)}} \right\rangle \\
&= \frac{1}{V} \sum_{\substack{h,h' \\ h \neq h'}} \langle W_{h,c} W_{h',c} \exp[-i\mathbf{k} \cdot (\mathbf{r}_{h,c} - \mathbf{r}_{h',c})] \rangle \\
&+ \frac{1}{V} \sum_{\substack{h,h' \\ h \neq h'}} \langle W_{h,c} \exp[-i\mathbf{k} \cdot (\mathbf{r}_{h,c} - \mathbf{r}_{h',c})] \rangle \sum_{s' \in h'} W_{h',s'} \hat{u}_{\text{sat},h'}(-k) \\
&+ \frac{1}{V} \sum_{\substack{h,h' \\ h \neq h'}} \langle W_{h',c} \exp[-i\mathbf{k} \cdot (\mathbf{r}_{h,c} - \mathbf{r}_{h',c})] \rangle \sum_{s \in h} W_{h,s} \hat{u}_{\text{sat},h}(k) \\
&+ \frac{1}{V} \sum_{\substack{h,h' \\ h \neq h'}} \langle \exp[i\mathbf{k} \cdot (\mathbf{r}_{h',c} - \mathbf{r}_{h,c})] \rangle \sum_{s \in h} W_{h,s} \hat{u}_{\text{sat},h}(k) \sum_{s' \in h'} W_{h',s'} \hat{u}_{\text{sat},h'}(-k). \tag{B6}
\end{aligned}$$

Note that cc refers to the complex conjugate. On large scales such that $k \rightarrow 0$, $\hat{u}_{\text{sat},h}(k) \rightarrow 1$, we have

$$\begin{aligned}
P_{2h,w}(k \rightarrow 0) &= \frac{1}{V} \left\langle \sum_{\substack{h,h' \\ h \neq h'}} (W_{h,c} + \sum_{s \in h} W_{h,s}) (W_{h',c} + \sum_{s' \in h'} W_{h',s'}) \exp[-i\mathbf{k} \cdot (\mathbf{r}_{h,c} - \mathbf{r}_{h',c})] \right\rangle \\
&= \frac{1}{V} \left\langle \sum_{\substack{h,h' \\ h \neq h'}} W_h W_{h'} \exp[-i\mathbf{k} \cdot (\mathbf{r}_{h,c} - \mathbf{r}_{h',c})] \right\rangle, \\
&= P_{2h,w}^{\text{halo}}, \tag{B7}
\end{aligned}$$

such that the power spectrum is equivalent to the 2-halo term of the halo power spectrum. In the opposite limit of $k \rightarrow \infty$, the 2-halo term $P_{2h} \rightarrow 0$, since $P_{hh'} \rightarrow 0$ due to halo exclusion.

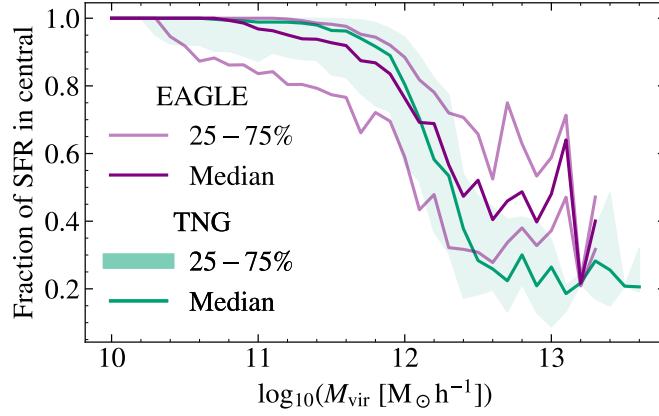


Figure C1. Fraction of the halo’s total SFR that occurs in the central galaxy as a function of the halo’s virial mass at $z \sim 1.5$. *Solid lines* are the median relation, with EAGLE shown in *purple*, and TNG in *green*. *Faint purple lines* include the 25th-75th percentiles for EAGLE; the *green shading* is the same but for TNG. In both simulations, central galaxies dominate the halo SFR in haloes with $\log M_{\text{vir}} \lesssim 11.5$, but contribute only of order 50 percent to the SFR for haloes with mass $\log M_{\text{vir}} \gtrsim 12.5$. In these more massive haloes, a fraction of SFR in the central galaxy is higher in EAGLE than in TNG. The scatter around the median relation is quite large in both cases. The transition from central-dominated SFR to a larger contribution from satellites is more sudden in TNG.

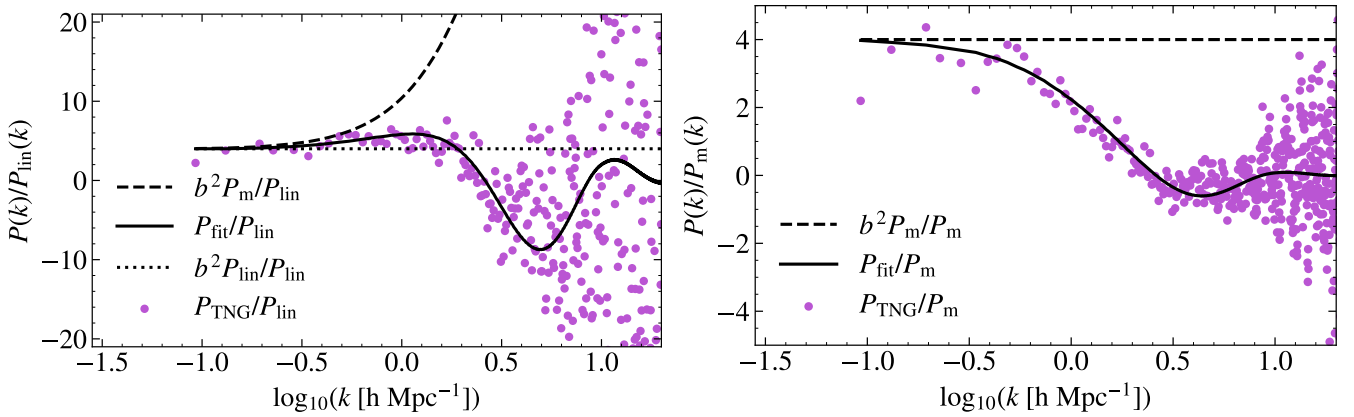


Figure C2. As Fig. 16, but for EAGLE. The fit to the 2-halo term (*solid line*) developed for TNG works equally well for EAGLE.

APPENDIX C: COMPARISON BETWEEN ILLUSTRITNG AND EAGLE

C1 SFR fraction in central galaxy

In Section 3, we plotted the average SFR contributed by central and galaxies as a function of the host halo mass for TNG. Here we compare this relation to that found in the EAGLE simulation.

Figure C1 compares the fraction of SFR in the central galaxy as a function of halo mass for TNG100-1 and EAGLE RefL100N1504. For EAGLE, the fraction also decreases as the halo mass increases, as AGN feedback quenches the central galaxy’s SFR and satellite subhaloes become more massive and hence have a higher SFR. The reduction in the central’s SFR contribution with increasing M_{vir} is more sudden in TNG than in EAGLE.

TNG implements two modes of feedback, a thermal mode that mimics quasar feedback, and a kinetic mode that mimics radio-mode feedback. The kinetic mode is more efficient and switches on at a black hole mass of $\sim 10^8 M_{\odot}$, causing stronger quenching of central galaxies. The sudden increase in AGN feedback efficiency as the black hole passes this mass threshold may contribute to the sudden decrease in the SFR of central galaxies. The EAGLE AGN feedback scheme is always thermal. At higher masses, the reduction in the contribution of the central galaxy to SFR is lower in EAGLE than in TNG. These results agree with the findings by Piotrowska et al. (2022) (see their fig. 3).

C2 Fit of 2-halo term in EAGLE

Figure C2 is the equivalent of Fig. 16 but with the dots representing the 2-halo term measured in the EAGLE simulation. The fit we proposed in Section 5.1, with the same parameters, also works reasonably well to reproduce the power spectrum observed in EAGLE.

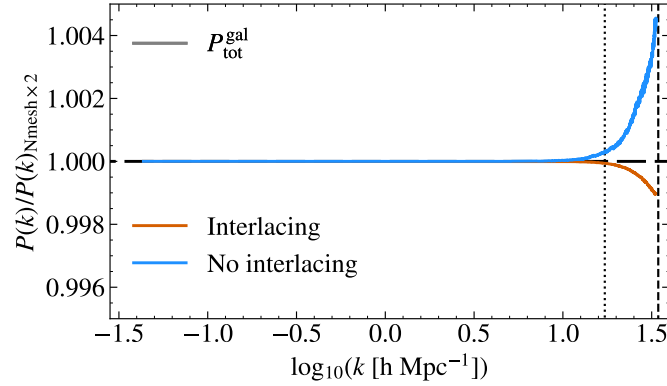


Figure D1. Ratio of the power spectra computed on a mesh with the fiducial resolution relative to that on a mesh with twice the resolution. The *orange lines* represent the power spectrum where interlacing has been used, whereas for the *blue points* interlacing has not been used. The *dashed vertical line* represents the Nyquist frequency, $k_{\text{Nyq}} = \pi N_{\text{mesh}}/L_{\text{box}}$, for the fiducial resolution and the dotted vertical line represents $k_{\text{Nyq}}/2$.

APPENDIX D: NUMERICAL DETAILS FOR CALCULATING SIMULATION POWER SPECTRA

We use NBODYKIT (Hand et al. 2019) for computing the power spectrum of a simulation. This involves interpolating the mass associated with discrete simulation particles to a regular mesh and then computing the power spectrum using a discrete Fourier transform.

How the mass is assigned to the mesh may affect the power spectrum on scales of a few mesh cells. In this paper, we adopt the triangular-shaped cloud interpolation scheme and correct for interlacing. The fiducial resolution of the mesh is taken to be approximately the SPHEREx linear resolution at $z = 1.5$ (corresponding to an angular resolution of $6.2''$), which is ~ 0.091 cMpc h^{-1} . This corresponds to using a mesh with N_{mesh}^3 cells, with $N_{\text{mesh}} = 2248$, for the TNG simulation with linear extent $L_{\text{mesh}} = 205$ cMpc h^{-1} . The Nyquist frequency is $k_{\text{Nyq}} = \pi N_{\text{mesh}}/L_{\text{mesh}} \approx 34.5$ h Mpc $^{-1}$. In the main text, we show all plots to $\log_{10}(k [\text{h Mpc}^{-1}]) \sim 1.3$, which is approximately half the Nyquist frequency. The small-scale power in the observations will additionally depend on the point spread function (see, e.g., Symons et al. (2021) for SPHEREx).

D1 Aliasing effects and interlacing

Aliasing effects become important close to the Nyquist frequency. The effect of aliasing is discussed in detail in Jing (2005). We adopt the interlacing option provided by NBODYKIT to correct for them. An explanation of this technique is detailed in Section 3.1 of Sefusatti et al. (2016).

Figure D1 shows the effect of interlacing. The reference power spectrum, $P_{N_{\text{mesh}} \times 2}$, uses $N_{\text{mesh}} = 2 \times 2248$ – i.e. twice our fiducial resolution. The Nyquist frequency for the reference mesh is higher, so aliasing effects are less significant at the Nyquist frequency of the fiducial mesh, therefore the reference power spectrum is closer to the ‘true’ power spectrum. The figure shows that the fiducial resolution reproduces the reference power spectrum better when the interlacing option is selected (orange line), than when it is not used (blue line). We therefore always use the interlacing option by default.

D2 Effect of the mass-assignment scheme

There exists a hierarchy of schemes for assigning the mass (or weight) of point particles to a mesh (see, e.g., Hockney & Eastwood 1981). Lower-order schemes (for example Nearest Grid Point, NGP) are numerically faster than higher-order schemes (such as Cloud In Cell, CIC, or Triangular-Shaped Cloud, TSC). Higher order interpolation schemes provide more accurate results at the expense of higher computational cost (Hockney & Eastwood 1981; Hand et al. 2019).

Figure D2 shows the ratio of the power spectra obtained from the NGP, CIC and TSC schemes on meshes with the fiducial resolution ($N_{\text{mesh}} = 2248$) relative to the reference power spectrum $N_{\text{mesh}} = 4496$ using TSC. At k_{Nyq} of the fiducial mesh (vertical dotted black line), the CIC and TSC schemes show differences smaller than 1.5 and 0.1 per cent with the reference power spectrum. The NGP scheme shows a much larger difference of more than 40 per cent. Even at $k_{\text{Nyq}}/2$, the NGP scheme still differs by ~ 15 per cent from the reference result, whereas CIC and TCS differ by only 0.2 and 0.1 per cent. In this paper, we adopt the TSC interpolation scheme. Even higher order schemes such as the PieceWise Cubic Spline (PCS) can be adopted if higher accuracy is required.

CIC or TSC interpolation can be thought of as a convolution of the particle density field (a sum of Dirac delta functions) with a smooth assignment kernel. NBODYKIT deconvolves the density field with this kernel when selecting the option `compensated = True`. We apply deconvolution throughout this paper.

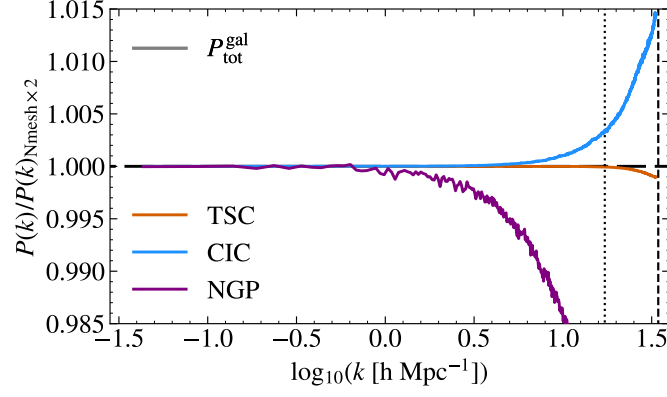


Figure D2. Ratio of the power spectra computed on meshes with the fiducial resolution, interpolated using the TSC (*orange*), CIC (*blue*) and NGP (*purple*) assignment schemes relative to a reference power spectrum computed on a mesh with twice the resolution. Interlacing has been applied in the computation of all the power spectra. Except for the NGP case, deconvolution has also been applied. The vertical lines are the same as in Fig. D2. In this paper we adopt the TSC scheme with interlacing and kernel deconvolution.